AN EXPERIMENTAL STUDY OF CO$_2$ EXSOLUTION AND RELATIVE PERMEABILITY MEASUREMENTS DURING CO$_2$ SATURATED WATER DEPRESSURIZATION

A REPORT SUBMITTED TO THE DEPARTMENT OF ENERGY RESOURCES ENGINEERING

OF STANFORD UNIVERSITY

IN PARTIAL FULFILLMENT OF THE REQUIREMENTS FOR THE DEGREE OF MASTER OF SCIENCE

By
Lin Zuo
June 2011

I certify that I have read this report and that in my opinion it is fully adequate, in scope and in quality, as partial fulfillment of the degree of Master of Science in Energy Resources Engineering.

_____

Prof. Sally M. Benson

(Principal Advisor)

Abstract

Dissolution of CO_2 into brine is an important and favorable trapping mechanism for geologic storage of CO_2. There are scenarios, however, where dissolved CO_2 may migrate out of the storage reservoir. Under these conditions, CO_2 will exsolve from solution during depressurization of the brine, leading to the formation of separate CO_2 phase. For example, a CO_2 sequestration system with a brine-permeable caprock may be favoured to allow for pressure relief in the sequestration reservoir. In this case, CO_2-rich brine may be transported upwards along a pressure gradient caused by CO_2 injection. Here we conduct an experimental study of CO_2 exsolution to observe the behaviour of exsolved gas under a wide range of depressurization.

Exsolution experiments in highly permeable Berea sandstones and low permeability Mount Simon sandstones are presented. Using X-ray CT scanning, the evolution of gas phase CO_2 and its spatial distribution is observed. Additionally, we measure relative permeability curves for exsolved CO_2 and water based on mass balances and continuous observation of the pressure drop across the core from 12.41MPa to 2.76MPa.

The results show that the minimum CO_2 saturation at which CO_2 bubbles mobilize is from 11.7%~15.5%. Exsolved CO_2 is distributed uniformly in homogeneous rock samples with no statistical correlation between porosity and CO_2 saturation observed. No gravitational redistribution of exsolved CO_2 is observed after depressurization. Also, significant differences exist between the relative permeability of exsolved CO_2 and water and the relative permeability derived from steady-state core flooding experiments. Specifically, low relative permeabilities of both CO_2 and water are measured, even when the CO_2 saturation is as high as 40%. The large mobility reduction is considered the result of disconnected gas bubbles in this two-phase flow system. This feature is also thought to be favorable for storage security after injection.

Acknowledgments

Contents

List of Tables

List of Figures

Chapter 1

1. Introduction and Literature Review

1.1. Carbon Capture and Sequestration (CCS)

Carbon dioxide capture and sequestration (CCS) is one of several key approaches to reduce greenhouse gas emission thus to stop the growth of greenhouse gas concentrations in atmosphere and global warming. CCS technologies involve three parts, gas separation, transportation and storage/sequestration. In sequestration sites, compressed CO_2 gas is injected into geological formations at depths where the hydrostatic pressure is above the critical pressure to take advantage of the high density of supercritical CO_2 (e.g. 0.61g/mL at 12.41MPa, 50^oC). Even with such a large density increase in subsurface, the density of CO_2 is still much less than water/brine, which makes the injected CO_2 phase subject to a strong buoyancy force and has the potential of moving upward. This migration trend of CO_2 plume is structurally stopped by a low permeability caprock on top of the storage reservoir and this trapping mechanism is referred to as the structural trapping. Many studies have been conducted regarding CO_2 migration in the storage reservoir including CO_2 plume development in a two-phase flow system, the effects of permeability and capillary pressure barriers on CO_2 migrations and strategies to minimize this unfavorable CO_2 movement (Hesse et al. 2006; Silin et al. 2008; Riaz et al. 2006; Juanes et al. 2006; Saadatpoor et al. 2010; Benson et al. 2005, 2008; Zhang et al. 2004).

1.2. Solubility Trapping

Besides structural trapping, over time, a certain fraction of CO_2 in the subsurface will dissolve in brine, owning to the high solubility of CO_2 in brine. This trapping mechanism is referred to as the solubility trapping. Carbon dioxide solubility in water/ brine is high and it increases linearly with pressure till the supercritical pressure is reached. At 12.41MPa and 50^oC, in pure water, the mass fraction of dissolved CO_2 approaches 5%.

Efforts have also focused on the fate of dissolved CO_2 in the storage reservoir (King et al. 2005; Leonenko et al. 2008; Hassanzadeh et al. 2007; Farajzadeh et al. 2007). In particular, studies have demonstrated that gravitational instability resulting from the slightly higher density of CO_2 saturated brine will lead to the development of convection currents which can accelerate plume dissolution, leading to improved storage security. However, much less effort has focused on the fate of dissolved CO_2 if it moves upward due to injection-induced pressure gradients between the storage reservoir and the overburden.

In general, the high solubility of CO_2 in water/brine is favorable for long-term sequestration since dissolved CO_2 is no longer subject to upwards buoyancy forces. As a result, solubility trapping is more secure than structural trapping and provides a transition pathway to permanent mineral trapping. Although estimates for the time needed for complete dissolution vary from 100's to 10,000's years (Riaz and Tchelepi 2008), depending on the permeability, geometry, temperature and salinity of sequestration sites, in many cases a substantial amount of injected CO_2 will dissolve over time in subsurface. While dissolved CO_2 provides better storage security, risks of leakage still exist. Once CO_2 saturated water/brine is depressurized, the solubility of CO_2 decreases and CO_2 exsolves from solution, expands and forms a separate phase as the fluid pressure continues dropping. This scenario is most likely to occur by vertical movement of CO_2 saturated fluids, triggered by an upward pressure gradient, either from overpressure from injection in deeper formations or underpressure of ground water due to pumping in a shallower formation. Carbon dioxide saturated fluids could permeate seals that are impermeable to the CO_2 phase in a two-phase system, and exsolve carbon dioxide at shallower depths. To understand the risks associated with CO_2 exsolution, this study seeks to observe the formation of exsolved CO_2 during depressurization and to assess the mobility of the CO_2 and water under these conditions.

2

1.3. Solution Gas Drive

There is a large body of knowledge about an analogous occurrence in oil reservoirs, the so-called process of solution gas drive. Gas bubbles exsolve from oil, grow and accumulate when reservoir pressure drops below the bubble point during primary depletion. The physical mechanisms of bubble formation (nucleation) and bubble growth in porous media are well studied in the context of solution gas drive. When pressure decreases, transient gas "nuclei" appear by thermal fluctuations (Wilt 1989). There are two different theories about the bubble formation in a porous medium. Li and Yortsos (1993) concluded that the most plausible nucleation mechanism in a porous medium with slow rate of pressure decline is "heterogeneous nucleation", which postulates various sites on solid surfaces become activated and bubbles arise once the local gas mass concentration is big enough to overcome the local capillary pressure. Then they described bubble growth during solution gas drive using a conventional convection-diffusion equation with some correction factors to account for the porous medium characteristics. Firoozabadi and Kashiev (1996) proposed an alternative "instantaneous nucleation" model for a sudden step change decrease in pressure and assume that in a given time the number of bubbles formed only depends on the supersaturation, the porous medium and fluid properties. Then all bubbles grow by diffusion. El Yousfi et al. (1997) conducted CO_2-water exsolution experiments in micro models with various pressure drops and concluded that the nucleation is "instantaneous", but bubbles form only when the pressure drop is big enough to balance the capillary force, which he described as a capillary threshold. He also found an approximate law for a spherical bubble growth (Hong and Woo 1985), correlating the bubble radius with the diffusion coefficient. The calculated values matched closely with the experimental data, and thus concluded that gas bubbles grow by diffusion.

Many experiments have been conducted to understand the flow properties of micro bubbles in solution gas drive. An important parameter identified in these experiments is the critical gas saturation, with reported values from 1% to 40% in various experiments (Firoozabadi 2001). The critical gas saturation is defined as the minimum gas saturation

at which evolved micro bubbles start behaving as a separate phase. In other words, the system enters a two-phase flow regime once the gas saturation grows above the critical gas saturation. Before approaching the critical gas saturation, the concept of simultaneous flow of oil and micro bubbles gas in solution or referred as "foamy oil" was first introduced by Smith (1988), but later rejected by experimental observations. Experiments show no gas production until the critical gas saturation is exceeded. After this, the gas flow is intermittent. Considering the mobility of a single bubble, the capillary pressure and the viscous pressure are relevant thus the characteristics of porous media, the properties of fluids and the flow rate are key causes for the wide spread of reported critical gas saturation values. Lower critical gas saturation values are observed with less viscous oils and with slower pressure decline rates. Low gas relative permeabilities were measured ($10^{-6} \sim 10^{-4}$) around the critical gas saturation in a system of exsolved gas and oil by Tang and Firoozabadi (2003), and Firoozabadi further concluded it is the high oil viscosity that contributes to the significant gas mobility reduction (2001).

Although solution gas drive provides a reasonable analogy for CO_2 exsolution, there are significant differences in both fluid properties and research focus. The high viscosity of oil is thought to be a major factor in solution gas drive mobility reduction. Heavy oil viscosity varies from 10^3 to 10^5cP while water has viscosity around 0.55cP at 50°C. The interfacial tension between oil and gas ranges from $0.1 \sim 5 \times 10^{-5}$N/cm, depending on temperature, pressure and oil composition, but the interfacial tension is an order of magnitude greater for CO_2-brine systems (e.g. 33×10^{-5}N/cm for water and CO_2 at 50°C and 12.41MPa (Georgiadis, et al. 2010)). Compared with oil/gas, in a CO_2/water system, due to the bigger interfacial tension, the work needed to form a spherical nucleus is larger thus a lower nucleation rate is expected under the same degree of super-saturation. Once micro-bubbles are formed, they are expected to be comparatively more mobile due to the low viscosity of water. Besides these differences in fluid properties, petroleum engineers have a much shorter time horizon than storage engineers.

In this study, several CO_2 exsolution experiments are conducted in four distinct rock samples, three Berea sandstones and one Mount Simon sandstone, with X-ray CT

4

scanning. Both rapid and slow depressurizations are applied to achieve CO_2 exsolution from CO_2 saturated water. The relative permeability curves of exsolved CO_2 and water were measured for the first time. Vertical migration and redistribution of CO_2 micro bubbles were also observed after equilibration.

Chapter 2

2. Methodology

CO_2 exsolution in a porous media is produced by lowering the pore pressure due to fluids extraction. The phenomena of exsolution is first observed by applying rapid pressure drops and later a slow depressurization approach is used to measure the critical gas saturation and the relative permeabilities of exsolved CO_2 and water. Then, the core is sealed to self-equilibrate and the migration and re-distribution of CO_2 during the equilibration is recorded to support the mobility measurements. The impact of sub-core heterogeneities is also investigated by correlating porosity and CO_2 saturation.

2.1. Experiment Setup and Equipment Description

The experimental facility used for these experiments is designed to conduct steady-state measurements of relative permeability curves for CO_2 and brine (Perrin and Benson, 2010). Small modifications, as described below, are made to accommodate these experiments. The basic facility shown in Fig.2-1 consists of the following components: an aluminum core holder surrounded with two electric heaters to maintain the rock sample at a constant temperature during the experiment (50^oC is used for these experiments); a confining pressure pump, connected to the core holder to provide a confining pressure outside the rock sample which is kept 2.76MPa higher than the pore pressure; a two phase separator with an ultrasonic transducer for fluid-fluid interface measurement; a backpressure pump serving as a reservoir to regulate the pressure of the whole system; two dual-pump systems, one for water and one for CO_2, each including two pumps attached with a set of programmable electric valves that synchronize pulling of one pump and refilling of the other to maintain a constant flow; a heater to warm fluids before entering the core holder. Logs of all pumps and the separator are collected

automatically. More detailed information about the facility can be found in Perrin and Benson (2010).
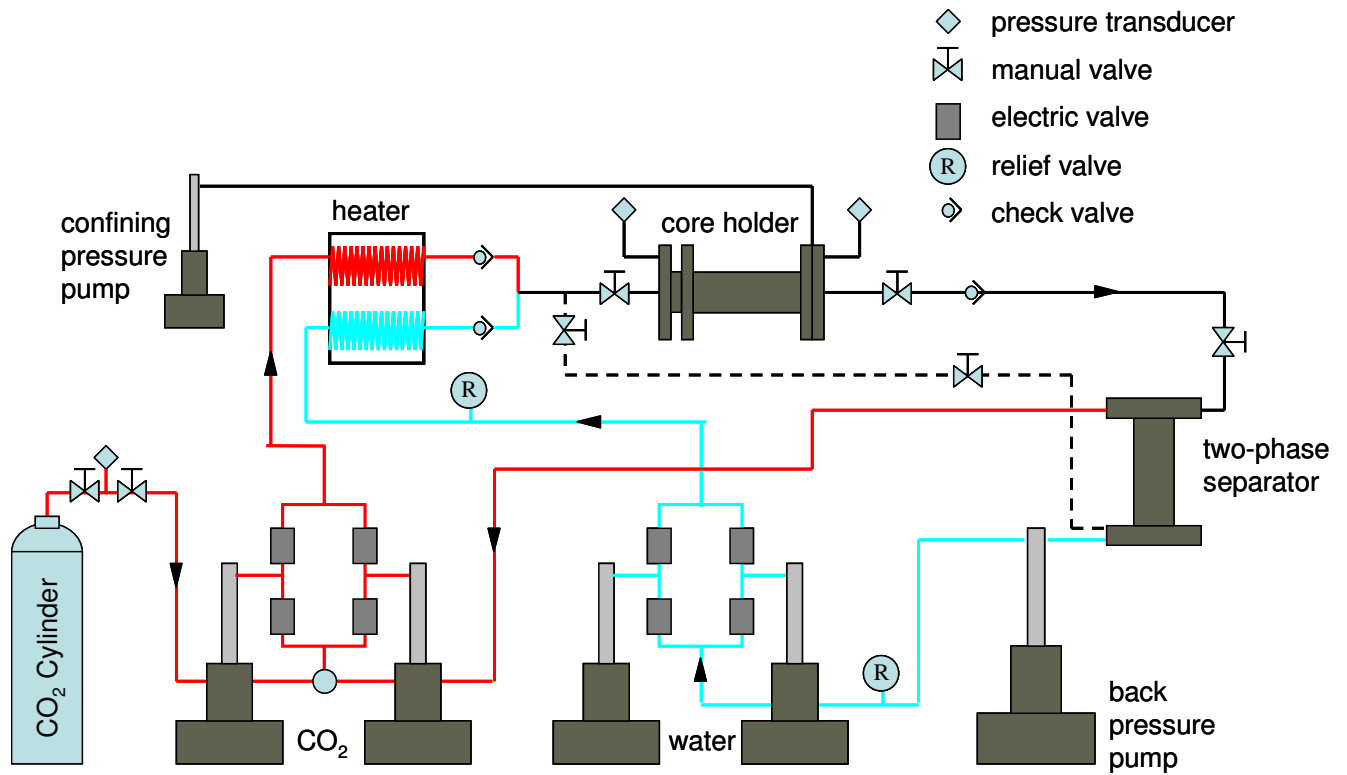
Figure 2-1: Experimental Setup for background scans and CO_2 saturated water preparation.

Rock samples are 2 inches ($\sim$ 5 cm) in diameter, dried in a vacuum oven before experiments, and then triple wrapped in 1) heat-shrinkable Teflon sleeve, 2) nickel foil (to prevent diffusion of CO_2 through the confining viton sleeve) and 3) a Teflon sleeve. A viton rubber sleeve separates the core from the confining fluid used to maintain realistic stresses in the rock (2.75MPa overpressure for these experiments).

An X-ray CT scanner is used to scan rock samples for measurements of porosity and CO_2 saturation by density difference and an overview of CT technology for imaging multiphase flow in porous media was given by Akin and Kovscek (2003). 2D images could be taken at a minimum interval of 1mm along the length of the rock sample and re-

constructed as a 3D image. The resolution of each 2D image is approximately 500 microns×500 microns per pixel.

2.2. Experiment Methods and Data Processing

By extracting fluids from a CO_2-water solution saturated rock sample at a constant temperature of $50^{\circ}C$, the pore pressure is reduced from 12.41MPa to produce solubility reduction and trigger CO_2 exsolution from the solution. After a CO_2-water solution saturated rock sample is prepared, a rapid pressure drop is applied to the rock sample to demonstrate exsolution due to pressure drops and also investigate the spatial distribution of exsolved CO_2 in porous media. Then, a slow depressurization is applied to measure the relative permeability curves of exsolved CO_2 and water. With this information, comparisons can be made with those from standard core flooding experiments and those from solution gas drive experiments. After the initial pressure drop, the core is sealed to observe the evolution of the CO_2 saturation towards gravity capillary equilibrium. Also, porosity and CO_2 saturation distributions are compared to discover any sub-core scale correlation between saturation and porosity. A positive correlation was found in core flooding experiments (Perrin and Benson 2010), which indicates the strong influence of sub-core scale heterogeneities on displacement efficiency and channeling through a porous medium in a drainage process, but it hasn't been tested in exsolution experiments or solution gas drive experiments.

Moreover, four different rock samples of two rock types are used to understand the influence of rock properties, such as permeability, porosity and heterogeneity, on the exsolution phenomena. Two homogenous Berea sandstone samples and one heterogeneous Berea sandstone sample with various permeabilities and porosities are used. One Mount Simon sandstone sample with relatively low permeability is also tested. Capillary pressure curves for all of the rock samples are obtained before the experiments for a prediction of gravity capillary equilibrium and comparisons with experimental observations. The rock samples and different depressurization approaches used are listed in Table 2-1.

Table 2-1: Experiment arrangement and properties of the rock samples

Experiment #	Rock sample characteristics		Depressurization Approaches	Intermediate pressure stages
1	Berea sandstone homogeneous	k : 266mD; ϕ : 18.7%; 9.52cm in length	rapid	9.65MPa, 6.89MPa, 5.52MPa
2	Berea sandstone heterogeneous	k : 439mD; ϕ : 21.0%; 15.24cm in length	rapid	6.89MPa
3	Berea sandstone homogeneous	k : 963mD; ϕ : 22.7%; 10.16cm in length	slow: 0.01, 0.1, 2mL/min	8.27MPa, 5.52MPa
4	Same as #3	Same as #3	slow: 0.1, 2, 10mL/min	N/A
5	Mount Simon sandstone homogeneous	k :15.7mD; ϕ : 23.9%; 9.04cm in length	slow: 0.1, 8mL/min	N/A
6	Same as #5	Same as #5	slow: -27.6kPa (4psi)/min	N/A

2.2.1. Background Scans and CO_2 saturated water preparation

A dry scan of the rock core is taken before injecting CO_2 to displace air. A series of CO_2 background scans are then taken as the pore pressure is increased by injecting pure CO_2 into the core at progressively higher pressures. The system is then depressurized back to atmospheric pressure. Next, at least 10 pore volumes of fresh water are injected into the rock sample. The system is then re-pressurized to make sure that all of the pore space is completely filled with water. The absolute permeability of the rock sample is then determined by measuring the pressure drop across the core over a range of flow rates. A

water background scan is then taken when the pore pressure reaches 12.41MPa. The rock sample is sealed by closing valves at both ends of the core holder and is now ready to prepare for the exsolution experiment.

To prepare CO_2 saturated brine at elevated temperatures and pressures, CO_2 and brine are circulated through the system using a bypass loop around the core. The system is operated continuously for at least 12 hours to establish equilibrium between CO_2 and brine. Since the fluids are circulated in a closed system, the volume of CO_2 lost due to dissolution can be calculated from a mass balance based on logs of the backpressure pump, water pumps, CO_2 pumps and the two phase separator. Demonstration that equilibrium between the fluids is achieved is determined when the volume of separate phase CO_2 in the system stabilizes. Also, any possible leakage can be easily identified if the volume of CO_2 in the system decreases over the experiment.

Once the CO_2 and water are equilibrated, the core holder is reconnected to the pump filled with CO_2 saturated water. After pumping at least 10 pore volumes through the core, a scan is taken of the rock filled with the CO_2 saturated water. Since the CO_2 saturated water is denser than pure water, ~0.005g/cm^3 at 5% CO_2 mass fraction (Ohsumi et al. 1992), the scan normally observed is around one unit larger in CT number than the corresponding pure water scan and it equals 0.4~0.5% bulk density increase. After the scan, the pumps are stopped and the rock sample is sealed by closing all of the valves.

2.2.2. Depressurization

During the exsolution experiments the pressure is decreased from 12.41MPa to 2.76MPa, while maintaining a constant temperature of 50°C. In some experiments, several intermediate pressure stages are maintained to allow for equilibration. To depressurize the system, a closed route is formed including the core holder, the backpressure pump and the two-phase separator. Two different configurations are used, one withdrawing fluids as fast as possible from both ends of the rock sample (rapid depressurization, ~1MPa/min, shown in Fig.2-2, a) and the other withdrawing fluids from one end of the core holder at a sequence of constant rates (slow depressurization, ~20kPa/min, shown in Fig.2-2, b) or at

a constant pressure drop rate (slow depressurization, -27.6kPa (4psi)/min, shown in Fig.2-2, b). The confining pressure is maintained in the range of 1.38~2.76MPa higher than the pore pressure during the depressurization process. Scans are also taken during the depressurization process. Once the pore pressure drops to a desired intermediate pressure, the backpressure pump is stopped, the core holder is sealed and multiple scans are taken. The depressurization is continued until the pore pressure drops to 2.76MPa.
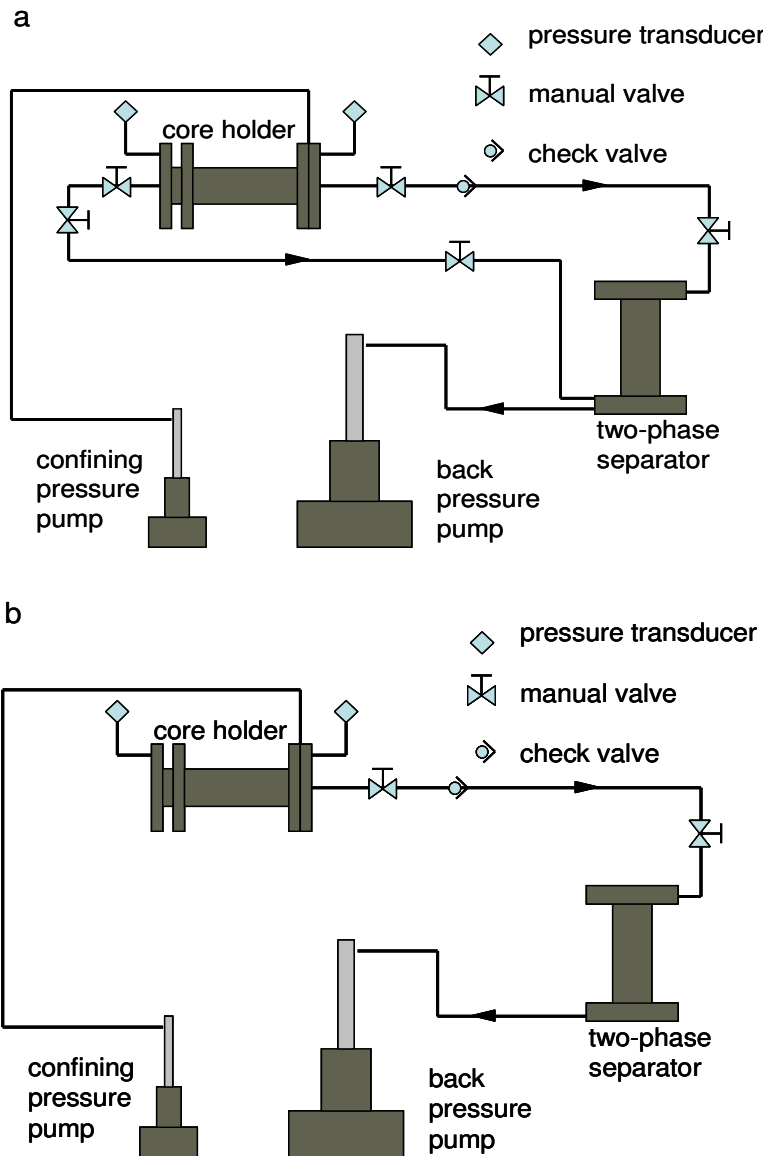

Figure 2-2: Experimental Setup for depressurization (a: rapid depressurization; b: slow depressurization).

2.2.3. Data Collection and Processing

Flow rates, pressures and fluid volumes in the pumps, pressures from two pressure transducers in the ends of the core holder are recorded every 3 seconds automatically by a programmed computer. The interface height in the two-phase separator is recorded every 21 seconds.

Images from the CT scanner have values depending on pixel density, normalized as -1000 for air and 0 for water. To obtain porosity, background scans of the dry core and water saturated core are needed. The porosity for each pixel is calculated as Eq.2-1:

$$\phi = \frac{CT_{water\ /\ rock} - CT_{air\ /\ rock}}{CT_{water} - CT_{air}} \tag{2-1}$$

where CT is determined by the scanner, and CT_{water}=0, CT_{air}=-1000. To determine the CO_2 saturation, background scans of the CO_2 saturated core at the appropriate pressure and CO_2-water solution saturated core are needed as well as an experiment scan of the multi-phase system. Scans of the CO_2 saturated core are taken at 9.65MPa, 8.27MPa, 6.89MPa, 5.52MPa and 2.76MPa. The CO_2 saturation of the experiment scan is calculated from Eq.2-2:

$$S_{CO_2} = \frac{CT_{solution/rock} - CT_{exp}}{CT_{solution/rock} - CT_{CO_2/rock}} \tag{2-2}$$

Core-average CO_2 saturations are calculated using core-average CT numbers of the CO_2 saturated core. The CO_2 saturated core was scanned only at several pressures and a quadratic fitting curve is used to interpolate the CT number of the CO_2 saturated core at a certain pressure, shown in Fig. 2-3. Slice-average CO_2 saturations are only calculated using slice-averaged CT numbers at pressures scans of the CO_2 saturated core were taken. CT numbers of the water saturated core and the CO_2-water solution saturated core are considered constant at different pressures owning to the incompressibility of water. For the 2-D porosity and CO_2 saturation maps, 10 individual scans are taken for each slice of the background scans of the CO_2 saturated core, CO_2-water solution saturated core and the experiment scan. Then, each pixel CT number used for the calculation is an average

of all pixels of multiple scans at the same position. By doing this, the random error of CT scanning is reduced to $\pm 2\%$ for each pixel value in terms of CO_2 saturation. The random error of slice-average and core-average CO_2 saturations is less than $\pm 0.1\%$.
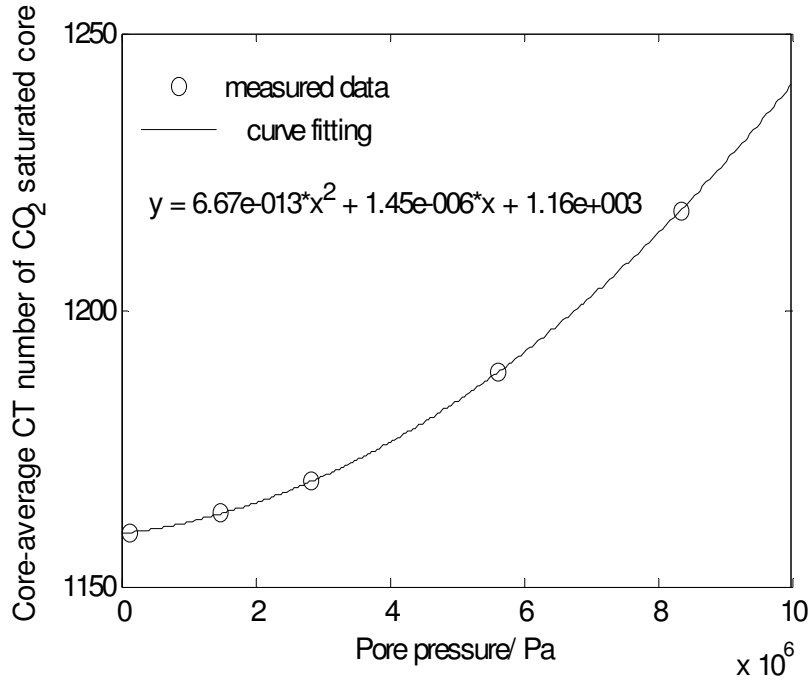
Figure 2-3: Core-average CT numbers of CO_2 saturated core versus pore pressures and the quadratic fitting curve.

2.3. Derivation of Relative Permeability

Based on Darcy's Law, a mathematical derivation is introduced for measuring relative permeabilities of exsolved CO_2 and water in an unconventional setup. Fluids are extracted from one end of the core while the other end is sealed and there is a no-flow boundary. The fluid properties are assumed to be constant across the rock sample. Even though there is a slight pressure drop along the core (the driving force for flow), it's so small that it produces negligible variation in fluid properties, such as density, viscosity and interfacial tension. For example, in the experiments, the average pore pressure is on the order of 1MPa while the pressure drop is on the order of 1~10kpa. The second assumption is that there is no significant CO_2 saturation gradient across rock samples,

14

which is demonstrated by the experiments, except in case of low CO_2 saturations. With the second assumption, we can assume the core is in a pseudo steady state for saturation, which means $\partial S / \partial t = const$ along the core. Porosity of the core is also assumed to be constant along the length of the core. The effects of these assumptions on relative permeability curve measurements are discussed later.

The following mathematical derivation for the calculation of relative permeability of water and exsolved CO_2 is based on Darcy's Law. A similar derivation can be found in Tang and Firoozabadi (2003).

For water phase, Darcy's Law without gravity is expressed as:

$$u = -\frac{kk_r}{\mu}\nabla p \tag{2-3}$$

In a one dimensional case:

$$u_x = -\frac{kk_r}{\mu}\frac{\partial p}{\partial x} \tag{2-4}$$

Integrate the pressure drop along a core with length of L:

$$\Delta p_w = -\frac{\mu_w}{kk_{rw}}\int_0^L u_{x,w}dx \tag{2-5}$$

The continuity equation for the water phase is expressed as:

$$\frac{\partial(\rho\phi S_w)}{\partial t} + \nabla \cdot (\rho u) = 0 \tag{2-6}$$

In a one dimensional case:

$$\frac{\partial(\rho\phi S_w)}{\partial t} + \frac{\partial(\rho u)}{\partial x} = 0 \tag{2-7}$$

Assume the water density is constant:

$$\phi\frac{\partial(S_w)}{\partial t} + \frac{\partial(u_w)}{\partial x} = 0 \tag{2-8}$$

$\dfrac{\partial(S_w)}{\partial t}$ doesn't change with x in a pseudo steady state:

$$u_w(x) = -\phi \frac{\partial(S_w)}{\partial t} \int\limits_0^x dx \tag{2-9}$$

When x=L:

$$u_w(L) = -\phi \frac{\partial(S_w)}{\partial t} L \tag{2-10}$$

Then substitute Eq. 2-9 and 2-10 into Eq. 2-5:

$$\Delta p_w = -\frac{\mu_w}{kk_{rw}} \int\limits_0^L (-\phi \frac{\partial(S_w)}{\partial t} \int\limits_0^x dx) dx = \frac{\mu_w}{kk_{rw}} \frac{\phi \partial(S_w)}{\partial t} \frac{L^2}{2} = -\frac{\mu_w L}{2kk_{rw}} u_w(L) = -\frac{\mu_w L}{2kk_{rw}} \frac{q_w}{A} \tag{2-11}$$

Then, the water relative permeability can be calculated as:

$$k_{rw} = \frac{\mu_w L q_w}{2Ak\Delta p_w} \tag{2-12}$$

For gas phase, Darcy's Law without gravity is expressed as:

$$u = -\frac{kk_r}{\mu} \nabla p \tag{2-13}$$

In a one dimensional case:

$$u_x = -\frac{kk_r}{\mu} \frac{\partial p}{\partial x} \tag{2-14}$$

Integrate the pressure drop along a core with length of L:

$$\Delta p_g = -\frac{\mu_g}{kk_{rg}} \int\limits_0^L u_{x,g} dx \tag{2-15}$$

The continuity equation for the gas phase:

$$\frac{\partial(\rho_g \phi S_g)}{\partial t} + \nabla \cdot (\rho_g u_g) = 0 \tag{2-16}$$

16

In a one dimensional case:

$$\frac{\partial(\rho_g \phi S_g)}{\partial t} + \frac{\partial(\rho_g u_g)}{\partial x} = 0 \tag{2-17}$$

Eq. 2-17 can be expressed as:

$$\phi(S_g \frac{\partial \rho_g}{\partial t} + \rho_g \frac{\partial S_g}{\partial t}) + (\frac{\partial \rho_g}{\partial x} u_g + \frac{\partial u_g}{\partial x} \rho_g) = 0 \tag{2-18}$$

Set:

$$a = \phi(S_g \frac{\partial \rho_g}{\partial t} + \rho_g \frac{\partial S_g}{\partial t}) \tag{2-19}$$

Assume the pseudo steady state:

$$\frac{\partial a}{\partial x} = 0 \tag{2-20}$$

For the third term on the left hand side of Eq. A-16:

$$\frac{\partial \rho_g}{\partial x} = \frac{\partial \rho_g}{\partial p} \cdot \frac{\partial p}{\partial x} = \rho_g C_g \cdot \frac{\partial p}{\partial x} \approx 0 \tag{2-21}$$

Then Eq. 2-18 can be written as:

$$a + \frac{\partial u_g}{\partial x} \rho_g = 0 \tag{2-22}$$

Given Eq. 2-20 and 2-22, integrate u_g from 0 to L:

$$u_g(x) = -a \int_0^x \frac{1}{\rho_g} dx = -\frac{a}{\rho_g} \int_0^x dx \tag{2-23}$$

When x=L:

$$u_g(L) = -\frac{a}{\rho_g} L \tag{2-24}$$

Then substitute Eq. 2-23 and 2-24 into Eq. 2-15:

$$\Delta p_g = -\frac{\mu_g}{kk_{rg}}\int_0^L u_{x,g}\,dx = -\frac{\mu_g}{kk_{rg}}\int_0^L (-\frac{a}{\rho_g}\int_0^x dx)dx = -\frac{\mu_g L}{2kk_{rg}}\frac{q_g}{A} \qquad (2\text{-}25)$$

The gas relative permeability can be calculated as:

$$k_{rg} = \frac{\mu_g L q_g}{2Ak\Delta p_g} \qquad (2\text{-}26)$$

With Eq. 2-12 and 2-26, the relative permeabilities of water and exsolved CO_2 can be calculated from measured parameters, such as the absolute permeability of the rock sample, pressure drop, flow rates and the rock sample dimensions.

The absolute permeability of the rock sample is measured before the depressurization process by water flooding. The pressure drop is measured directly by two pressure transducer at each end of the core holder and the water pressure drop and the gas pressure drop are assumed to be equal ($\Delta p_g = \Delta p_w$). To measure flow rates, two scans are needed, one at time t_1, one at time t_2, $t_2 > t_1$. The average water flow rate between t_1 and t_2 is calculated from Eq.2-27:

$$q_w = \frac{S_{w1} - S_{w2}}{t_2 - t_1} \cdot V_p \qquad (2\text{-}27)$$

where V_p is the pore volume of the core.

And the average CO_2 flow rate between t_1 and t_2 is calculated as Eq. 2-28:

$$q_{CO_2} = \frac{S_{CO_2,1} \cdot \rho_{CO_2,1} / \rho_{CO_2,2} + S_{w1} \cdot \Delta / \rho_{CO_2,2} - S_{CO_2,2}}{t_2 - t_1} \cdot V_p \qquad (2\text{-}28)$$

where Δ [CO_2 mass/water volume] is the CO_2 solubility change between $p_1(t_1)$ and $p_2(t_2)$. This formula accounts for the expansion of the CO_2 originally in place and additional exsolved CO_2.

Chapter 3

3. Experimental Results

Carbon dioxide exsolution is produced by extracting fluids from a core with CO_2-water solution. First, experiments are conducted with rapid depressurization to observe the evidence of CO_2 exsolution under this mechanism and the distribution of exsolved CO_2 in a porous media. Later, experiments are conducted with a slow depressurization approach which produces CO_2 exsolution at a relatively constant pressure drop rate (~20kPa/min) with a sequence of constant rates and at a constant pressure drop rate (27.6kPa (4psi)/min) with a constant pressure drop control. The critical gas saturation and the relative permeability curves of exsolved CO_2 and water are measured with the slow depressurization approach. After the pore pressure drops to 2.76MPa, the rock sample is sealed to observe the evolution of gravity capillary equilibrium to support the previous mobility measurements. The correlation between CO_2 saturation and porosity is also investigated at the sub-core scale after the pressure drops to the final stage.

3.1. Evidence for the Development of Exsolved Phase

One homogeneous Berea sandstone and one heterogeneous Berea sandstone are used to conduct exsolution experiments with the rapid depressurization approach. Rock samples are initially filled with CO_2 saturated water at $50\,^{o}C$ and 12.41MPa. Afterwards, fluids are extracted as fast as possible until the pressure drops to a specified pressure. The rock sample is then sealed and monitored for 6 to 24 hours to observe equilibration of exsolved CO_2 under the influence of gravity and capillary forces until the depressurization process starts again.

Significant amounts of exsolved CO_2 are observed in these experiments. Fig.3-1 shows the slice-averaged CO_2 saturation varying with pressure and equilibrium time (5~24 hours) for the homogeneous rock sample (a) and the heterogeneous one (b). Fig.3-2

shows the corresponding slice-averaged porosity curves for both samples. The highest CO_2 saturations in both experiments reached over 40% due to solubility reduction and CO_2 expansion as the pressure drops. CO_2 saturation gradients are also observed, especially in the heterogeneous rock sample. Saturation gradients in the homogeneous rock sample are most likely caused by preferential flow from one end of the core holder rather than equal flow from both ends during the depressurization process.
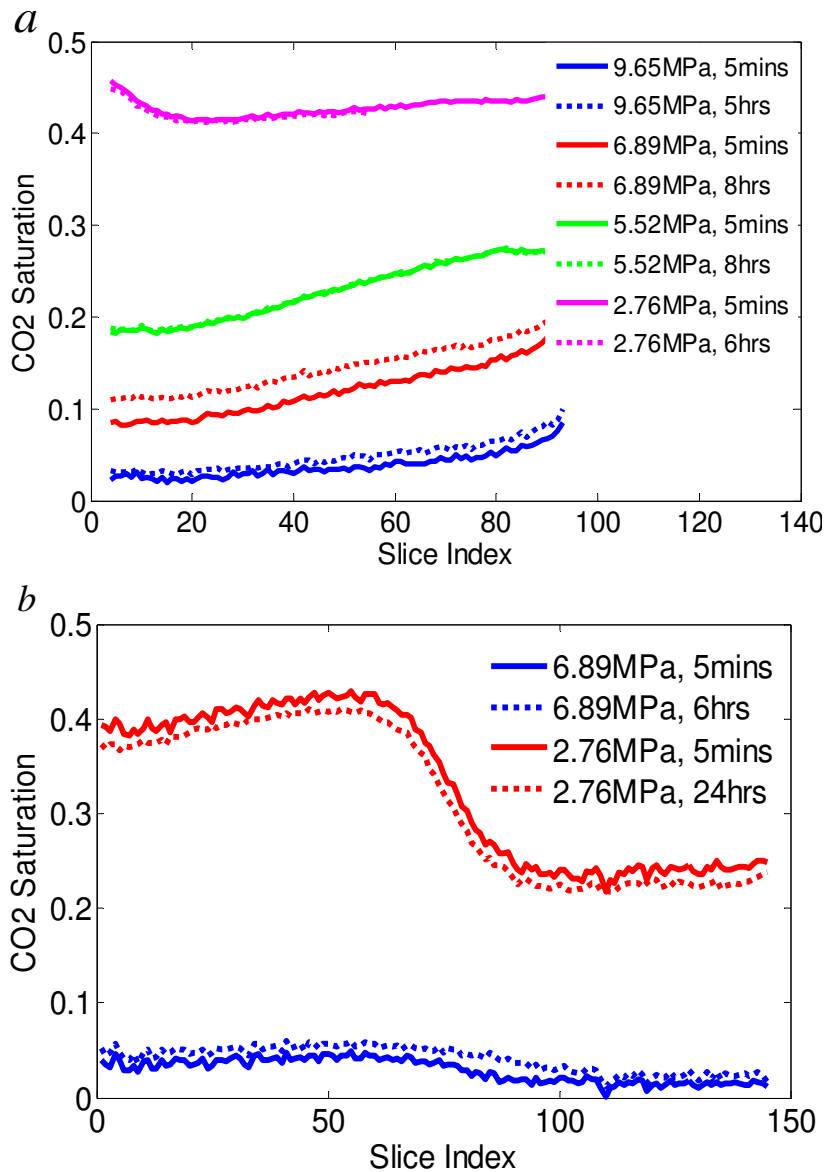

Figure 3-1: Slice-averaged CO_2 saturation under various pore pressures and equilibration times for the homogeneous rock sample (a) and the heterogeneous one (b).
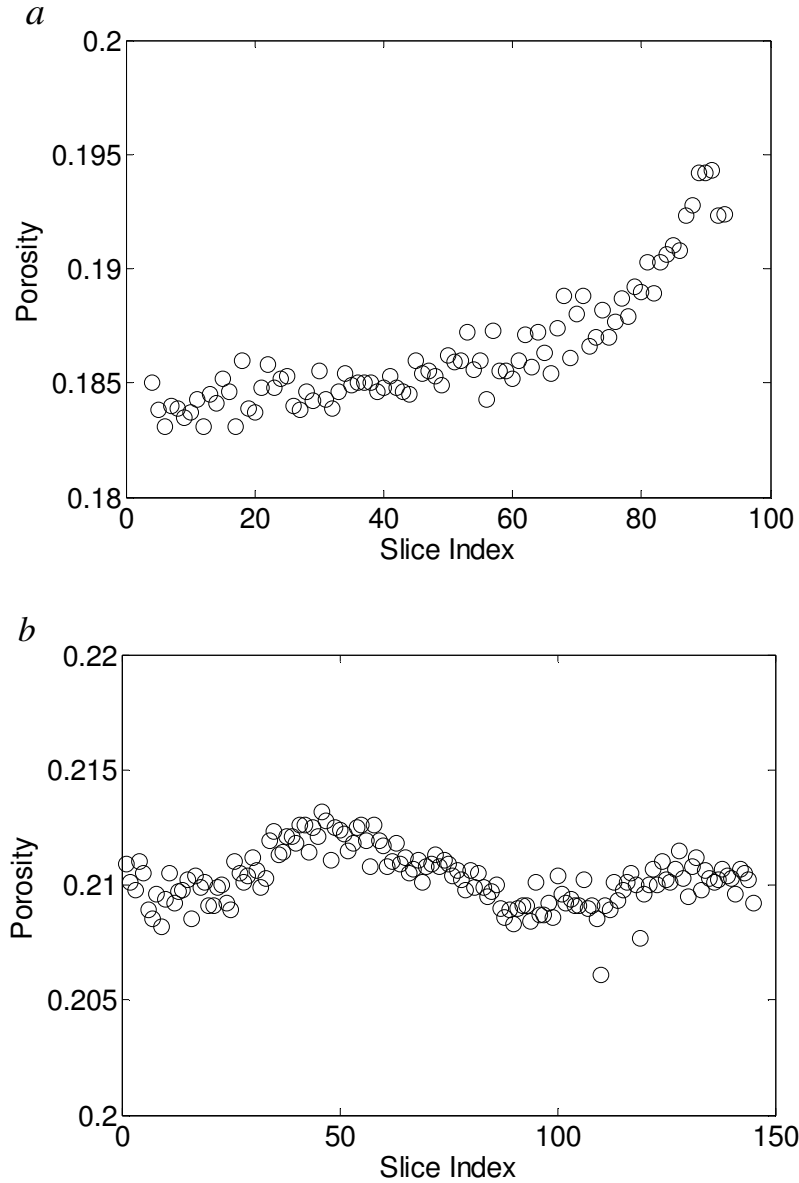
Figure 3-2: Slice-averaged porosity for the homogeneous rock sample (a) and the heterogeneous one (b).

The heterogeneity of rock samples also contributes to the variable CO_2 saturation. Fig.3-3 shows the re-constructed 3D porosity map (a) with the CO_2 saturation map (b) of the homogeneous rock sample and the porosity map (c) with the CO_2 saturation map (d) for the heterogeneous rock sample. The low porosity portion in the middle of the heterogeneous sample appears to have formed a flow barrier and amplified the flow preference. Compared with the results from the homogeneous rock sample which

presumably has the same preferential flow introduced by the experimental setup, the CO_2 saturation gradients in the heterogeneous rock sample mostly come from the sub-core scale heterogeneities.
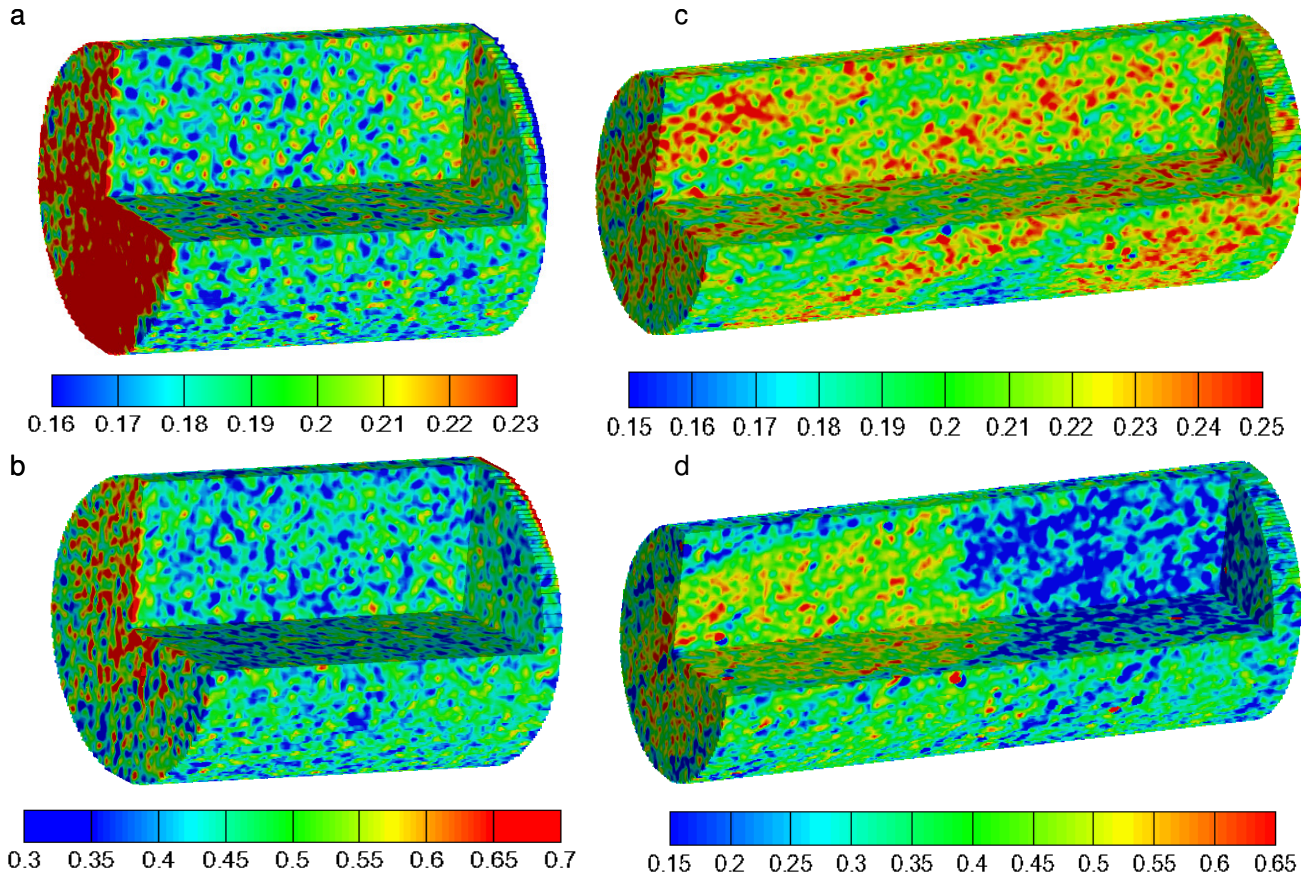
Figure 3-3: 3D reconstructed porosity and CO_2 saturation images: a) porosity of the homogeneous rock sample; b) porosity of the heterogeneous rock sample; c) CO_2 saturation of the homogeneous rock sample at 2.76MPa; d) CO_2 saturation of the heterogeneous rock sample at 2.76MPa

While these experiments clearly demonstrate the exsolution of CO_2, they provide little information about the mobility of exsolved CO_2. As a result, the slow depressurization approach is applied to derive the mobility of exsolved CO_2 and water.

3.2. The Mobility of Exsolved Phase

One homogeneous Berea sandstone and one Mount Simon sandstone are used to carry out exsolution experiments with slow depressurization rates. Rock samples are initially 50 ^{o}C and 12.41MPa and filled with CO_2 saturated water equilibrated at 50 ^{o}C and 11.03MPa. Fluids are extracted from one end of the core holder at a sequence of constant volumetric withdrawal rates until the pore pressure drops to a specified pressure. The rock sample is then sealed and the system is monitored for up to 260 hours to observe equilibration of exsolved CO_2 under the influence of gravity and capillary forces. In the depressurization process, the critical gas saturation is determined from the onset of amplified fluctuations in the pressure drop across the rock sample (Tang and Firoozabadi 2003, Tang et al. 2006). Four experiments are conducted with this method. One experiment (experiment #3) is conducted in a Berea sandstone with intermediate pressure stages of 8.27MPa and 5.52MPa, and another experiment (experiment #4) is conducted as a repetition of experiment #3 with a sequence of higher withdraw rates and without intermediate pressure stages. A third experiment (experiment #5) is conducted with a much lower permeability Mount Simon sandstone without intermediate pressure stages and a forth experiment (experiment #6) is conducted as a repetition of experiment #5 with a constant pressure drop and without intermediate pressure stages (see Table 2-1).

3.2.1. Relative Permeability Measurements

Measurements of the relative permeability of water and exsolved CO_2 are conducted based on Darcy's Law. Since fluids are withdrawn from one end of the core holder, the mathematical method described in Section 2.3. is applied for relative permeability calculation (Eq. 2-12 and Eq. 2-26) during the depressurization process.
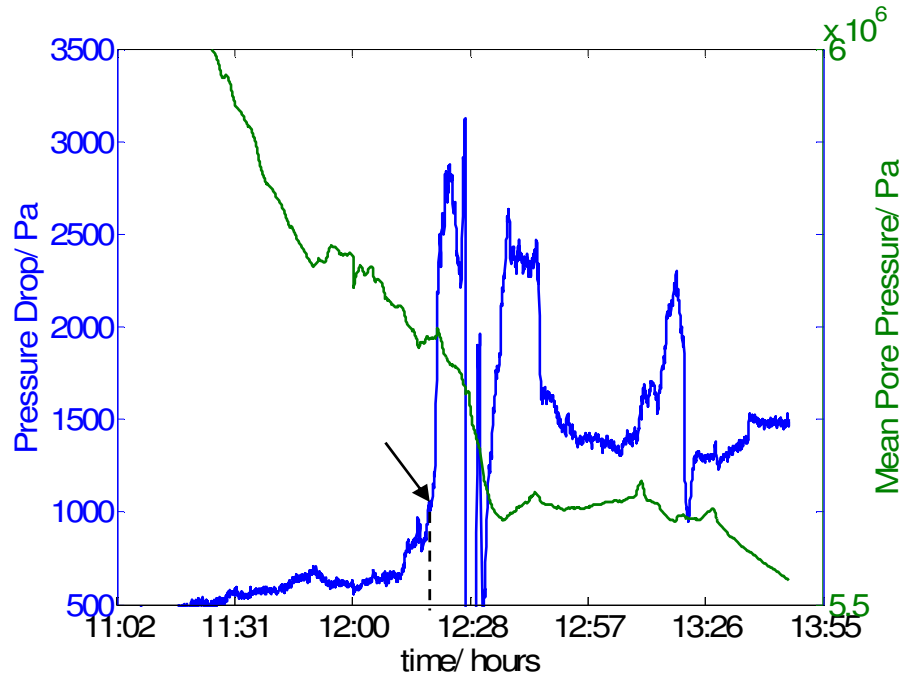
Figure 3-4: Mean pore pressure and the pressure drop in experiment #3 around the critical gas saturation. The critical gas saturation was determined by the onset of large pressure drop fluctuation, shown by arrow.

In experiment #3, #4 and #5, to start the depressurization process, the back pressure pump is set at a low and constant volumetric withdrawal rate. The pore pressure of the rock sample and the pressure drop across the rock sample are recorded continuously. At first the pressure drops very quickly due to the low compressibility of water. Once exsolved CO_2 forms, the withdrawal rate is increased to maintain a relatively constant pressure drop rate (~20kPa/min). Fig.3-4 shows the mean pore pressure and the pressure drop versus withdrawal time in experiment #3, where the critical point to mobile gas bubbles appeared around 12:20, corresponding to a CO_2 saturation of 11.7%. In experiment #4 and #5, the critical gas saturations are 15.5% and 11.9%, respectively.

In experiment #6, a constant pressure drop rate is applied to the back pressure pump and the corresponding critical gas saturation is 13.7%, shown in Fig. 3-5.
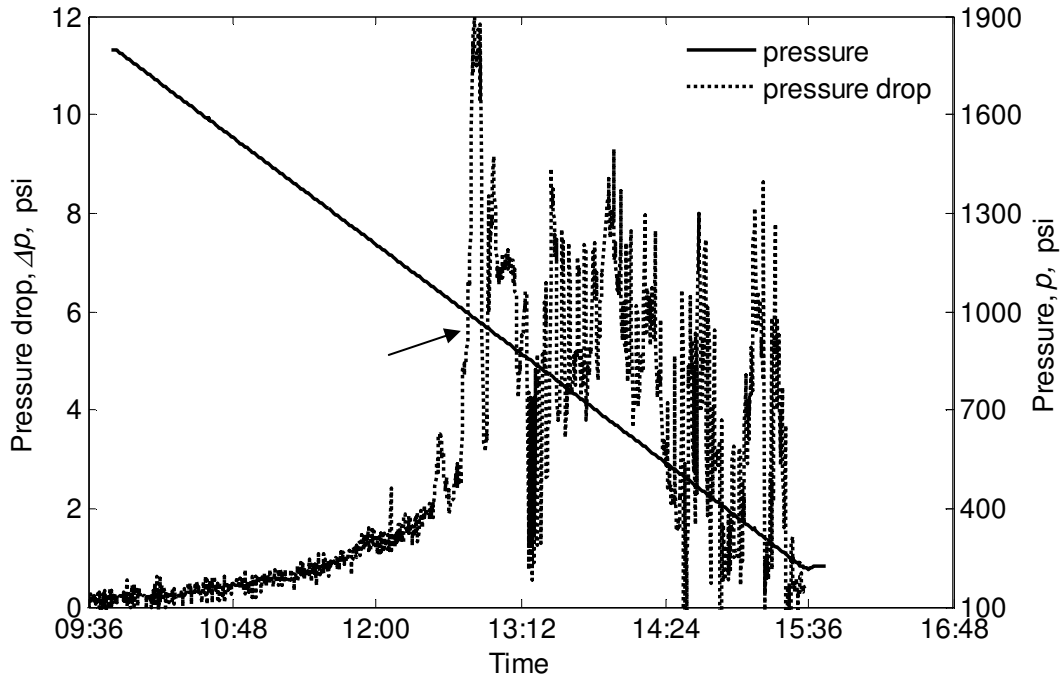
Figure 3-5: Mean pore pressure and the pressure drop in experiment #6. The critical gas saturation was determined by the onset of large pressure drop fluctuation, shown by arrow.

Fig.3-6 shows the pore pressure versus CO_2 saturation for experiment #3, #4 and #5, which are remarkably similar. However, by comparing experiments #3 and #4, it can be seen that the higher withdrawal rates lead to higher gas saturations. Fig.3-7, 3-8 and 3-9 show the pressure drop across rock samples, water flow rates and CO_2 flow rates versus CO_2 saturation in experiment #3, #4 and #5, respectively.

Figure 3-6: Pore pressure versus CO_2 saturation during the depressurization.
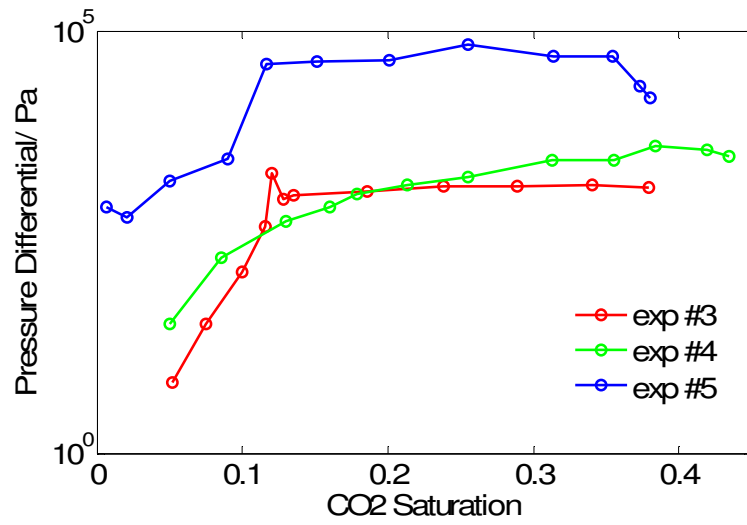
Figure 3-7: Pressure drop across the rock sample versus CO_2 saturation during the depressurization

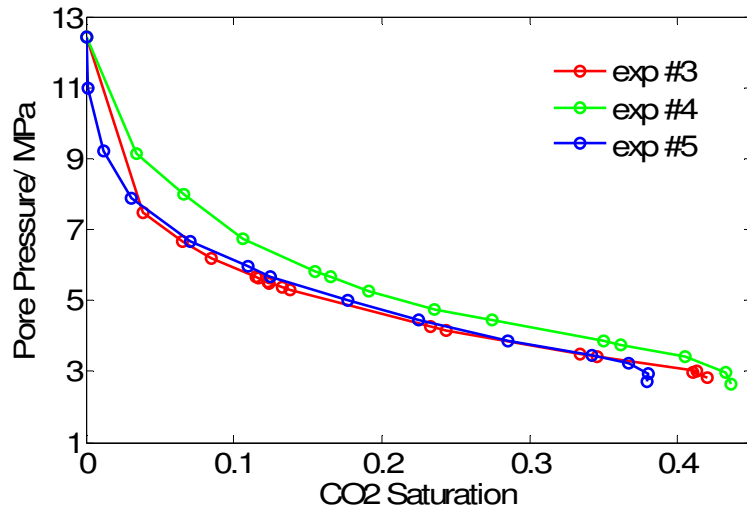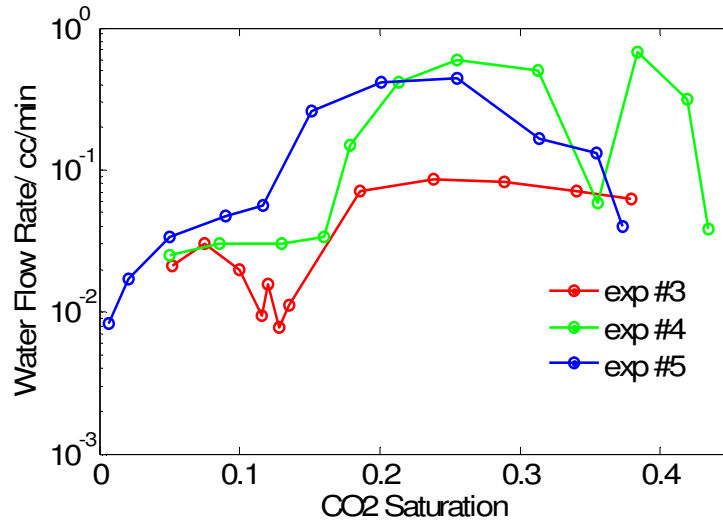Figure 3-8: Water flow rate versus CO_2 saturation during the depressurization.
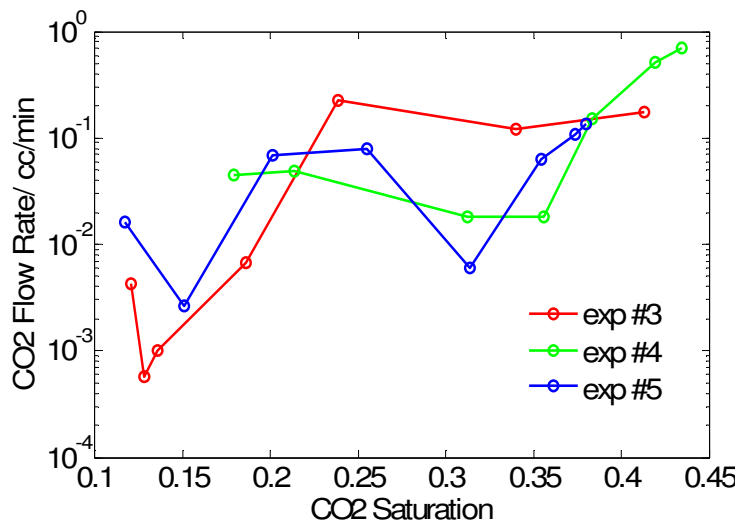
Figure 3-9: Exsolved CO_2 flow rate versus CO_2 saturation during the depressurization.

During depressurization, the rate of pore pressure decrease slowed as more gas exsolved. The pressure gradient across the samples increased as gas saturation increased until the critical gas saturation was reached. After the critical saturation was reached the pressure gradient across the sample remained relatively constant. The critical gas saturations corresponding to the turning points in the pressure gradients curves, ~12%, match well with the pressure transient data l, 11.7%~15.5%, where when gas bubbles became mobile,

the amplitude of pressure fluctuation increased as gas slugs mobilized intermittently. Flow rates of water and exsolved CO_2 increased as CO_2 saturation grew, but exhibited large fluctuations.

Fig.3-10 shows the relative permeability curves of exsolved CO_2 and water in experiment #3, #4 and #5. Fig.3-11 shows the relative permeability curves of exsolved CO_2 and water in experiment #6. The relative permeability data show very low mobility for both exsolved CO_2 and water. For the exsolved CO_2 phase, the relative permeability is in a range of 10^{-5} to 10^{-3} for CO_2 saturation of 10% to 40%, and for the water phase, the relative permeability drops rapidly as exsolved gas starts evolving, and continues dropping to less than 0.1 as the gas phase starts moving.
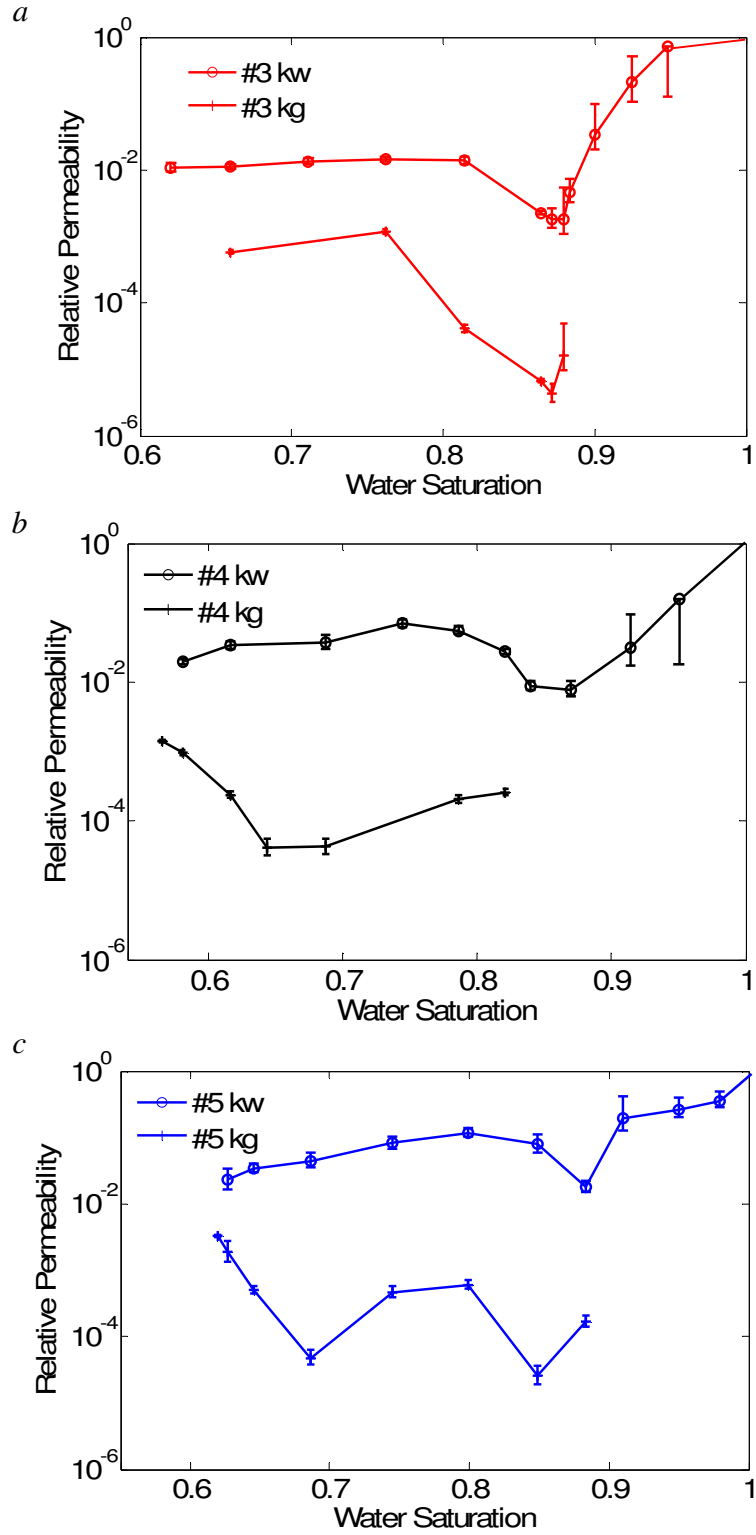
Figure 3-10: Relative permeability curves of exsolved CO_2 and water: a) experiment #3; b) experiment #4; c) experiment #5
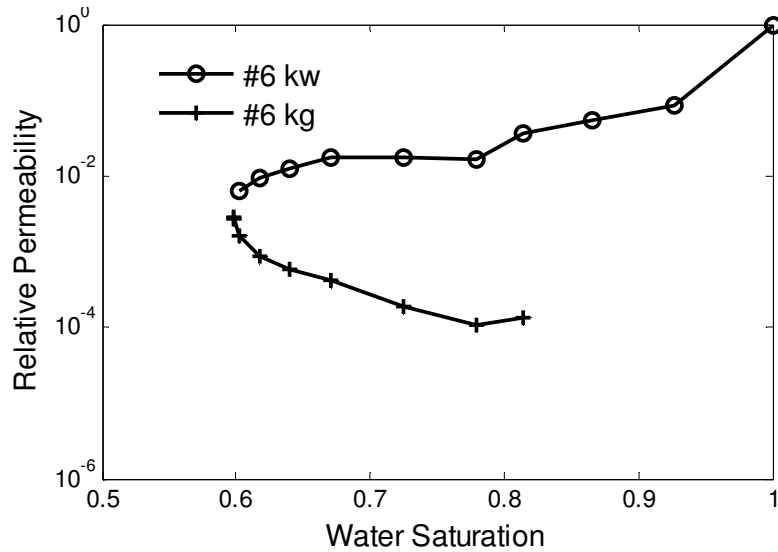
Figure 3-11: Relative permeability curves of exsolved CO_2 and water in experiment #6

3.2.2. Correlation between Porosity and CO_2 Saturation

Positive correlations between porosity and CO_2 saturation are often observed in standard core flooding experiments in both homogenous and heterogeneous rock samples at reservoir conditions (Perrin and Benson 2010; Krause et al., 2011). The spatial distribution of CO_2 is shown to be highly influenced by the sub-core scale heterogeneities. It is of great interest to investigate whether such influence on CO_2 distribution also exists in a system undergoing gas exsolution. If such a correlation does not exist, it indicates different flow processes between the flowing phases.

Fig.3-12 shows the averaged images of porosity (a) and CO_2 saturation (b) at the middle slice of the rock sample, #50, in experiment #3. Fig3-13 shows the scatter plots of porosity versus CO_2 saturation at the middle slice of the rock sample, #50, and two slice 20mm apart from the middle in experiment #3. The CO_2 saturation is measured at 2.76MPa immediately after the pressure drop. No significant correlation is observed between porosity and CO_2 saturation. Therefore, it appears that CO_2 is exsolved from solution uniformly regardless the variation of porosity during the pressure drop. The correlation coefficients, r^2, of the regression lines are 5e-3, 4.5e-3 and 9.8e-3 for slice #30, #50 and #70, respectively, showing no systematic correlation between the saturation

and porosity. It indicates CO_2 exsolves universally in a porous media and the sub-core heterogeneities and flow processes do not have big influences on the CO_2 saturation distribution in exsolution.
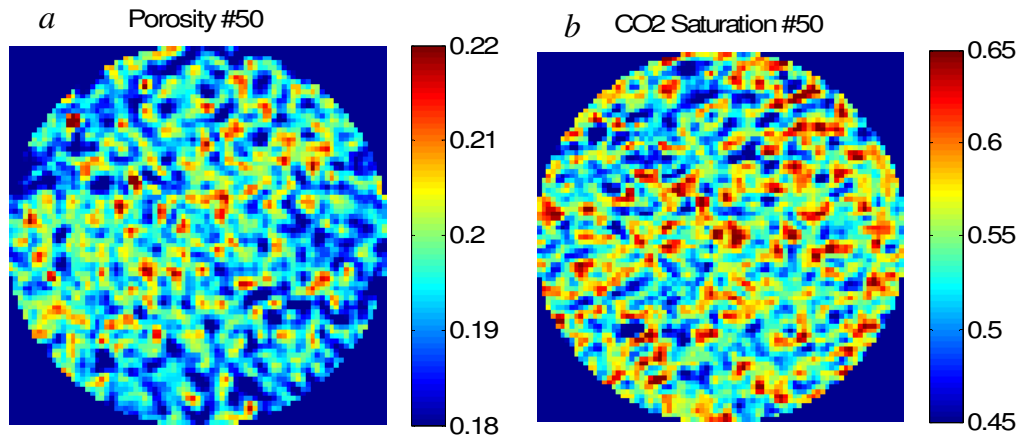
Figure 3-12: Averaged images of porosity (a) and CO_2 saturation (b, at 2.76MPa) at slice #50 in experiment #3.
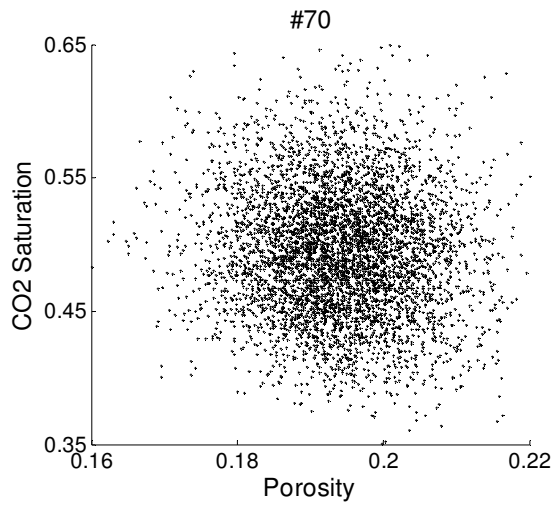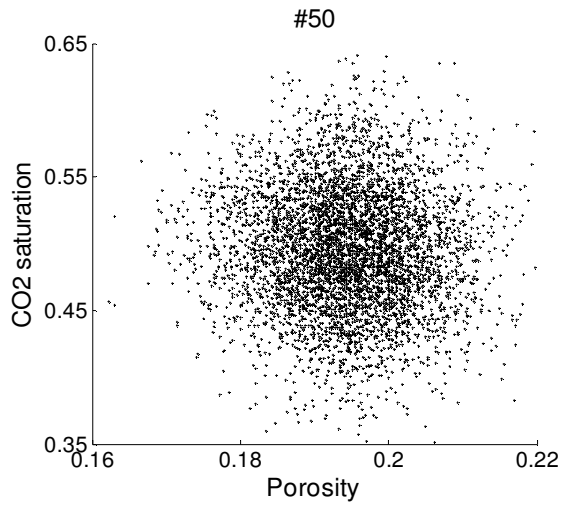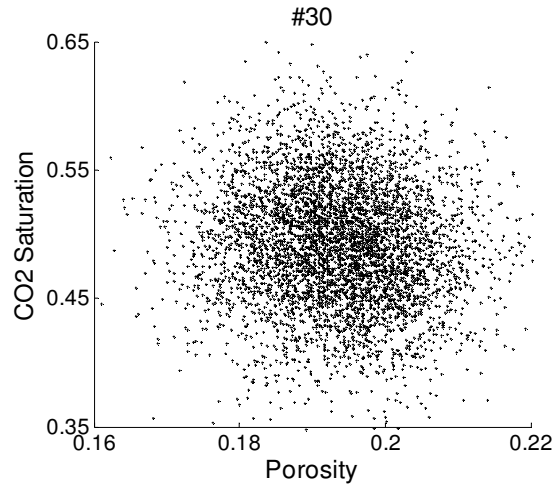
Figure 3-13: Scatter plots of porosity and CO_2 saturation at slice #30, #50, #70. CO_2 saturation was measured immediately after the pore pressure dropped to 2.76MPa in experiment #3.

Fig.3-14 shows the scatter plots of the initial CO_2 saturation and the CO_2 saturation measured 260 hours after the pore pressure dropped to 2.76MPa at slice #30, #50, #70 in experiment #3. During this period of time, the core holder is sealed and maintained at a constant temperature of 50^OC. It shows there is a good statistical correlation between CO_2 saturation before and after equilibrium. The correlation coefficients, r^2, of the regression lines are 0.805, 0.822 and 0.791 for slice #30, #50 and #70, respectively. This indicates no re-distribution of CO_2 is occurring over the 260 hour period. The exsolved CO_2 demonstrated a very low mobility and is consistent with the low relative permeability measurements.
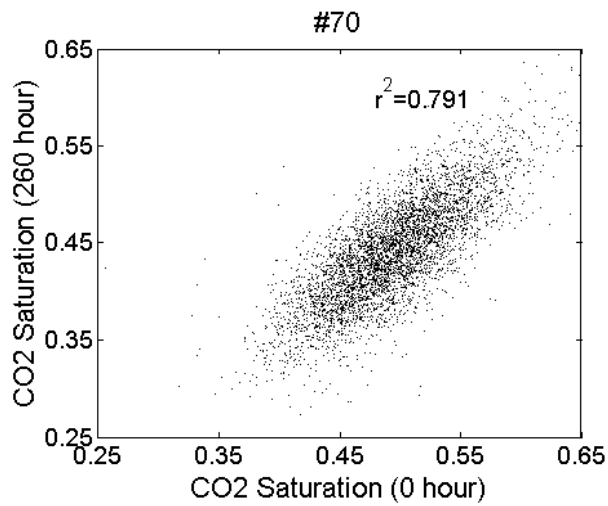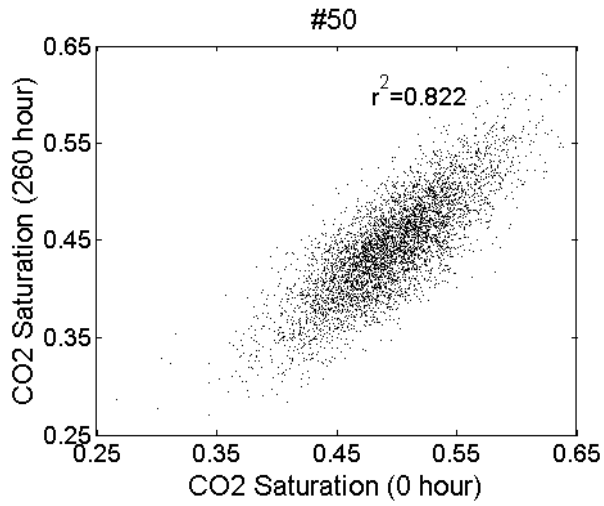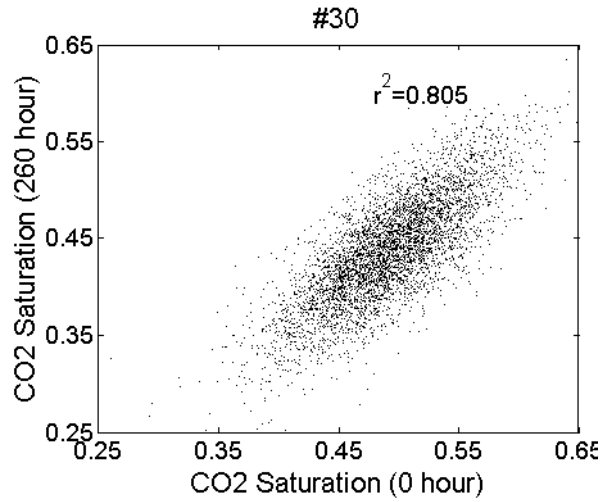
Figure 3-14: Scatter plots of the initial CO_2 saturation versus the saturation measured 260 hours after the pore pressure dropped to 2.76MPa at slice #30, #50, #70 in experiment #3.

Fig.3-15 shows the evolution of CO_2 saturation after 260 hours equilibration in experiment #3. Fig.3-15 a, c, e are the resulting saturation changes calculated by subtracting the CO_2 saturation immediately after the core is sealed from that of 16 hours, subtracting that of 16 hours from that of 100 hours and subtracting that of 100 hours from that of 260 hours. Fig.3-15 b, d, f are the corresponding scatter plots of CO_2 saturation change versus porosity. No statistical correlation between CO_2 saturation change in a pixel scale and porosity is shown in Fig.3-15 and therefore there is no redistribution preference in porosity in the rock sample. The correlation coefficients, r^2, of the regression lines (solid lines in) are 0.1, 0.08 and 0.13, respectively. Again, the sub-core scale heterogeneities do not have an impact on CO_2 redistribution.

The calculated average CO_2 saturation dropped around 5% in 260 hours, while the core holder is sealed and the pore pressure remains relative constant, 2.76MPa to 2.91MPa. An additional amount of 1.7mL water is needed to come into the core during the 260 hours to account for the 5% CO_2 saturation drop. Given the 2% measurement accuracy of CO_2 saturation in a pixel scale, there is basically no change in slice average CO_2 saturations during the equilibration.
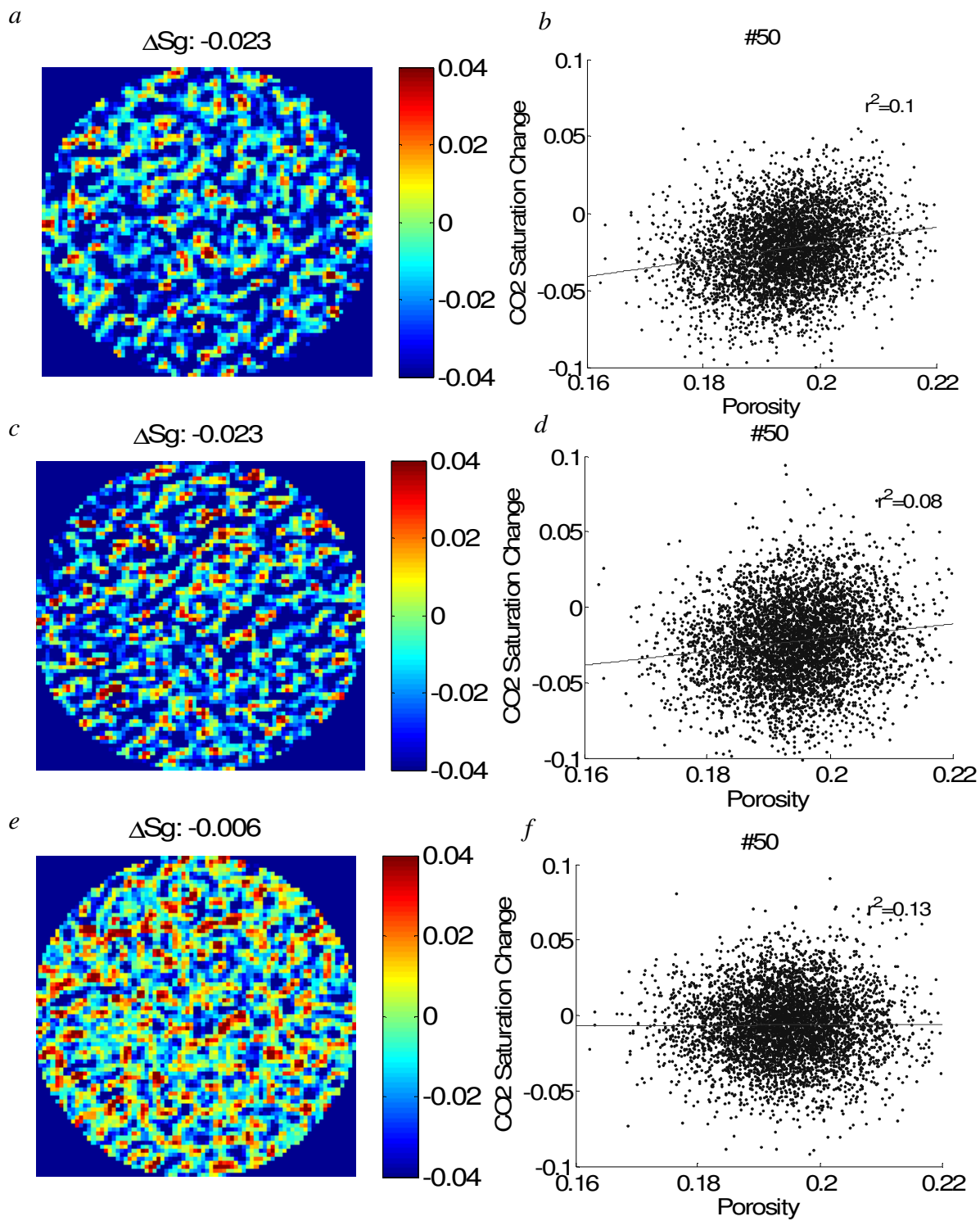
Figure 3-15: CO_2 saturation changes during the equilibrium period at slice #50 after the pore pressure dropped to 2.76MPa (a: 16hrs minus 0hr; c: 100hrs minus 16hrs; e: 260hrs minus 100hrs; b, d, f: the corresponding scatter plots of CO_2 saturation change versus porosity) in experiment #3.

3.2.3. *Gravity Effect on CO_2 Saturation Distribution*

Fig.3-16 shows the vertical distribution of CO_2 after the pore pressure is decreased to 2.76MPa at slices #30, #50 and #70 in experiment #3. CO_2 saturation at each height is obtained by averaging the center 16 pixels horizontally on the corresponding averaged images. The similarity in CO_2 saturation between 100 hours and 260 hours demonstrates that the saturation is only changing very slowly, if at all. These curves are compared to the saturation distribution expected for a homogeneous core allowed to achieve gravity-capillary equilibrium. The calculation is based on the measured capillary pressure curve shown in Fig.3-17 and assumes that the gravity capillary equilibrium is reached. Under these conditions, if the CO_2 is mobile, a vertical saturation gradient is expected. As shown by the experimental data, no vertical CO_2 gradient is observed, even after 260 hours of equilibration. This indicates that CO_2 bubbles are not sufficiently interconnected and mobile enough to reach the gravity capillary equilibrium over the observed time period.
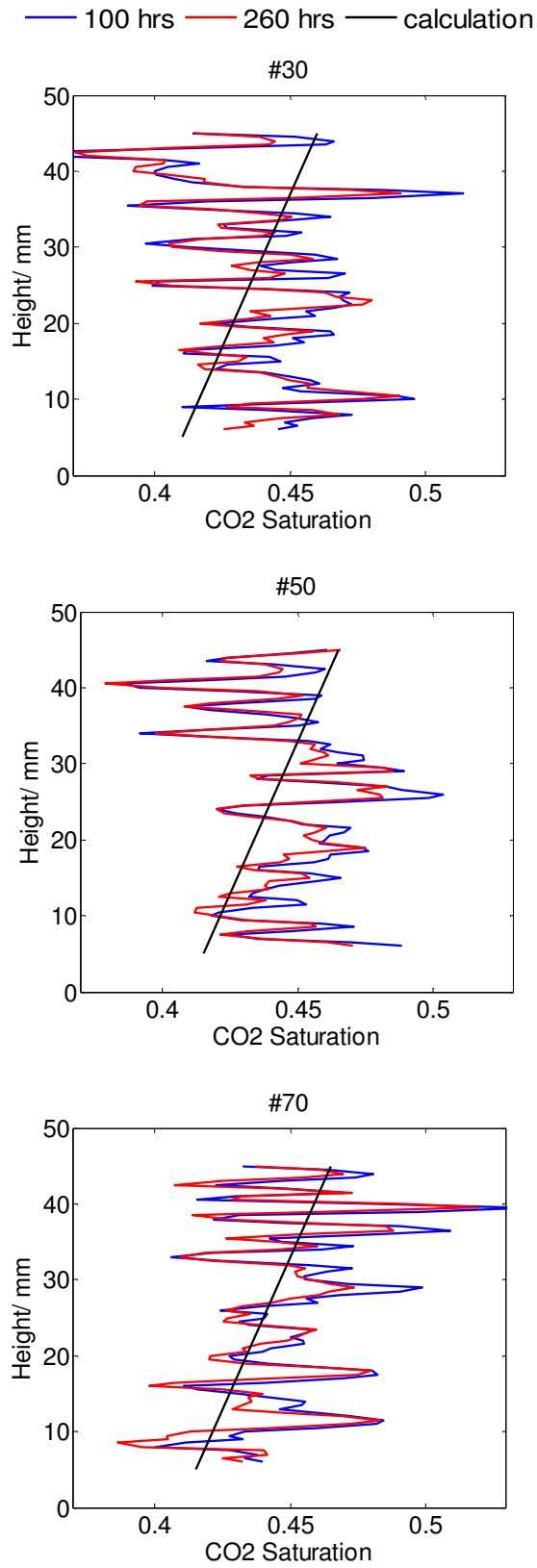
Figure 3-16: Vertical CO$_2$ distribution as equilibrium processed 100 hours (blue curves) and 260 hours (red curves) after the pore pressure dropped to 2.76MPa at slice #30, #50 and #70 in experiment #3.
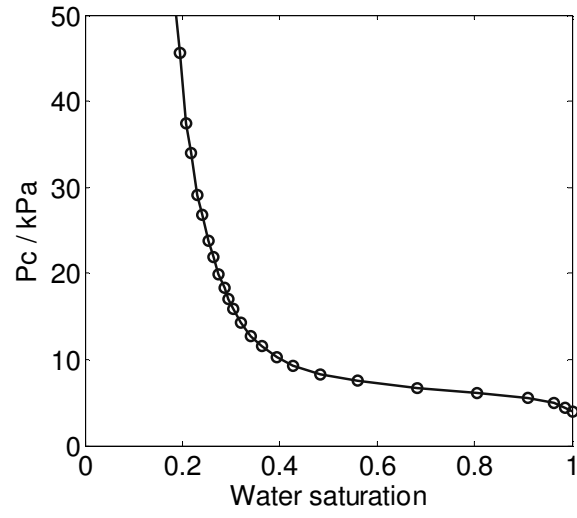
Figure 3-17: Capillary pressure curve measured using mercury porosimetry for the homogeneous
Berea sandstone used in experiment #3.

Chapter 4

4. Discussion

4.1. Mobility of exsolved CO_2

Three experiments are conducted with two distinct rock samples. In all cases, very low relative permeabilities of exsolved CO_2 ($10^{-5} \sim 10^{-3}$) are recorded even when the CO_2 saturation is over 40%. Over a period of 260 hours after exsolution, no systematic CO_2 re-distribution is observed either, further supporting the low mobility of CO_2.

The relative permeability curves of exsolved CO_2 and water are compared to standard steady-state measurements on the same cores. As shown in Fig.4-1, the relative permeability of exsolved CO_2 is far less than for the drainage relative permeability curves (a: Berea sandstone; b: Mount Simon sandstone). This indicates that in a system undergoing gas exsolution, even with small gas saturation, use of drainage relative permeability curves either from a standard core flooding experiments or an empirical correlation model could result in large deviations. Consequently, simulations would significantly overestimate the mobility and transport of exsolved CO_2. Also, the significant reduction in both water and CO_2 mobility observed in these experiments could be favorable for storage security after injection. The exsolved gas may form a permeability barrier, preventing CO_2 migration or even blocking possible leakage paths.
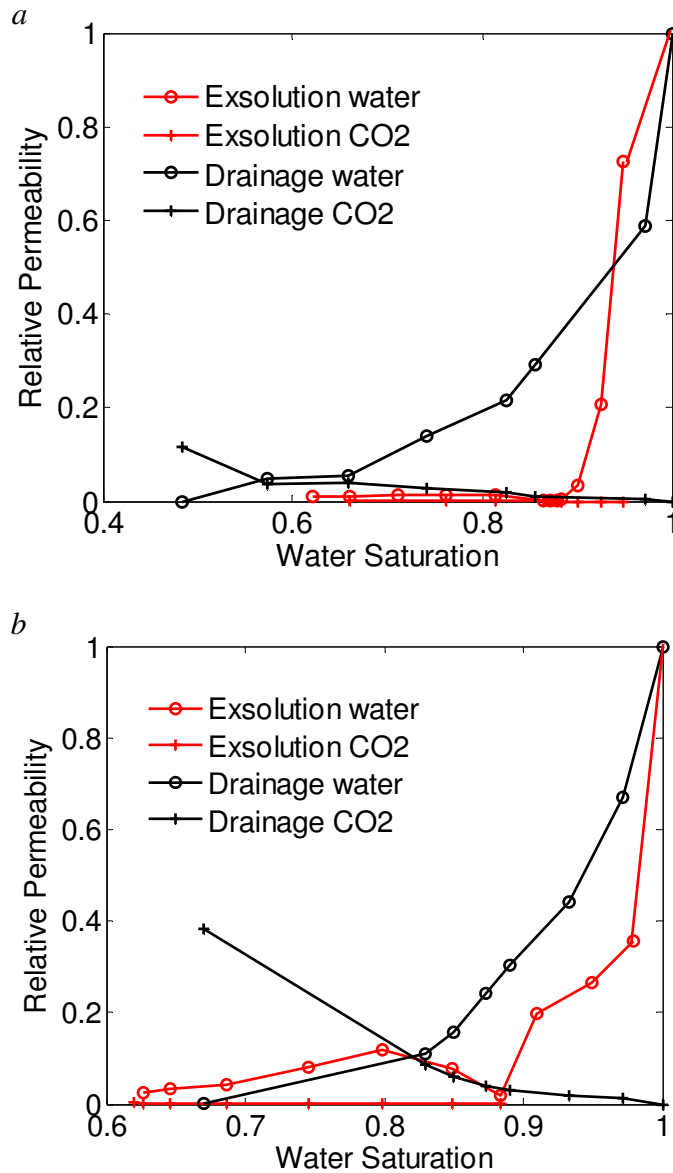
Figure 4-1: Comparison between relative permeability curves of exsolved CO_2 and water and standard steady-state core flooding experiments (a: Berea sandstone; b: Mount Simon sandstone).

The measured relative permeability of exsolved CO_2 is in the same range of that observed in solution gas drive experiments (Tang and Firoozabadi 2003, Tang et al. 2006). However, the argument that in solution gas drive the viscosity of heavy oil is largely responsible for significant gas mobility reduction is not relevant in the case of CO_2 exsolution, since water is much less viscous than heavy oil. In fact, Fig.3-7 shows that

before the gas bubbles become mobile, the flow resistance imposed by exsolved CO_2 increases exponentially with CO_2 saturation. This indicates that regardless of what kind of aggregation the gas phase has, a "trapped" gas phase is occupying the pore space, thus reducing the accessible flow paths and making it harder for the water to flow. Once the critical saturation is reached, the pressure drop no longer increases with gas saturation and the flow resistance decreases. This indicates the increasing volume of gas in pore space do not block the flow of water as much once they are mobile. We hypothesize that when the gas saturation is low, bubbles tend to, or be pushed by a pressure gradient to, occupy the space close to pore throats and have a significant impact on water flow. Once the critical saturation is reached and bubbles become mobile, the gas saturation increase mainly by expansion in pore bodies which do not have much influence on flows. This explains the pressure drop plateau after the critical saturation is reached shown in Fig.3-7. As the gas phase becomes mobile, pore throats are opened and reclosed intermittently due to the intermittent gas flow. As a result, the mobilities of both water and CO_2 phases remain very low. The presence of disconnected gas bubbles may be the main cause of low gas mobility. The bigger water mobility reduction may be caused by the relatively larger interfacial tension between water and CO_2, compared to heavy oil and gas in solution gas drive experiments.

Under normal two-phase flow conditions, gravity segregation will occur and the gravity capillary equilibrium will be approached over time when a density difference exists between wetting phase and non-wetting phase. However, this well-established theory may not apply to exsolved CO_2 since bubbles appear isolated in pores initially and do not become inter-connected, at least over the 260 hours observed here. Exsolved CO_2 may still be trapped even under very high CO_2 saturations, which is contrary to accepted understanding of two-phase flows, especially during drainage. However, this is not counter-intuitive since flow properties of a standard two-phase flow, such as relative permeability curves and capillary curves, are measured based on the continuum phase assumption which is not valid in an exsolution situation.

4.2. Errors in relative permeability measurements

These relative permeability measurements are based on the slow depressurization method which withdraws fluids from only one end of the core holder. The calculation is based on a simple mathematic derivation with two major assumptions: first, fluids are incompressible; second, there is no gas saturation gradient across rock samples. The density of CO_2 doesn't change much under the experiment conditions ($p \geq 2.76$MPa; $\Delta p \leq 0.01$MPa). The gas saturation gradients during depressurization in these experiments are less than 5% across the sample. As a result, the error from saturation gradients is relatively large when the pore pressure is high and the average gas saturation is low, but is less when the average gas saturation reaches 30%~40%.

The flow rates of water and exsolved CO_2 are calculated from X-ray CT images. The pixel value of each image is subject to random errors. By averaging 10 identical scans taken for each slice, both background scans and experiment scans, the STD of an averaged image is reduced to $1/\sqrt{10}$ of one single image, and the combined STD of CO_2 saturation is reduce to an absolute value of 2%. This accuracy applies to the observation in a pixel by pixel scale, such as the scatter plot of saturation versus porosity. In relative permeability measurements, the core average saturation is used and it is much more accurate than in a pixel by pixel scale. Thus, the flow rates were measured with errors less than $\pm 0.1\%$.

The largest errors come from the measured pressure drop across the rock. Since the depressurization process is slow and fluids' flow rates are small, the absolute pressure drop is small, especially at the beginning of measurements where the CO_2 saturation is low. Generally, a measurement taken in a less permeable rock sample with higher withdraw rates will improve the pressure drop accuracy.

4.3. Influence of depressurization approaches on CO_2 exsolution

Regarding the influence of depressurization on CO_2 exsolution, some differences are observed between rapid and slow depressurization approaches, shown in Table 2. The rapid depressurization results in higher CO_2 saturations under the same pore pressures, indicating that CO_2 is less mobile and more water was extracted from the rock samples at higher flow rates. This is consistent with observations from solution gas drive experiments (Tang et al. 2006). Under field conditions, the pore pressure drop could be even slower than the slow depressurization rate used here, and it could lead to a lower CO_2 saturation under the same pressure.

No statistical correlation between CO_2 saturation and porosity and no vertical saturation gradient were observed in experiments with both depressurization approaches. Qualitatively, exsolution and the resulting mobility reduction do not depend on the depressurization rate of the system. However, in terms of relative permeability measurements, the poor repetition of experiment #3 and #4, especially in CO_2 curves, is partially due to the difference of withdrawal rates applied to the system. Tang et al. (2006) also observed the same phenomenon in solution gas drive experiments that relative permeability measurement is sensitive to expansion rate in composite cores. The sparseness of data points is another reason for the poor repetition. Moreover, the critical gas saturation increased as the depressurization rate increased (11.7% in exp#3 and 15.5% in exp#4) and it is also consistent with observations from Li and Yortsos (1993) and Tang et al. (2006). Results from experiments of constant withdrawal rates and constant pressure drop rates are very much consistent except in the critical gas saturation region. In experiment #3, #4 and #5, a local minimum water relative permeability is observed close to the critical gas saturation (Fig. 3-10), but it doesn't exist in experiment #6 (Fig. 3-11). The local minimums of water relative permeability are artifacts caused by manually changing withdrawal rates when the critical gas saturation is approached and there are big errors associated with water flow rate calculation. A depressurization process with a constant pressure drop rate is recommended for relative permeability measurements.

Table 4-1: Comparison of CO$_2$ saturations at various mean pore pressures

	9.65MPa	6.89MPa	5.51MPa	2.76MPa
Rapid depressurization	3%~5%	10%~15%	20%~27%	40%~46%
Slow depressurization	N/A	6.5%~10%	13%~17%	41%~43%

Chapter 5

5. Conclusions and Future Work

A series of exsolution experiments have been conducted to understand the phenomenon of CO_2 exsolution associated with pressure drop and the flow properties of exsolved CO_2 and water. Conclusions drawn from these experiments are:

1. Significant amounts of CO_2 exsolve from solution as pore pressure drops, and the CO_2 saturation reaches up to 45% by a pressure drop from 12.41MPa to 2.76MPa at a constant temperature of 50°C. These experiments demonstrated a possible exsolution scenario and the reoccurrence of gas phase as CO_2 saturated brine moves upward.

2. The critical gas saturation of CO_2 exsolution is recorded as 11.7%~15.5%, depending on the depressurization rates and rock types. The recorded critical gas saturation values are within the range summarized by Firoozabadi (2001), 1%~40%, from solution gas drive experiments with various oil/gas compositions. A higher expansion rate results in a higher critical gas saturation. It is consistent with observations from solution gas drive studies.

3. CO_2 exsolves uniformly throughout the core and there is no statistical correlation between CO_2 saturation and porosity. This differs from the observation of core flooding experiments co-injecting CO_2 and water, in which a positive correlation was found (Perrin and Benson, 2010; Krause et al., 2011). A uniform CO_2 distribution is intuitively expected as exsolution occurs universally when pressure drops, though rock heterogeneity would produce flow preference during extraction from the core, but this is not observed.

4. No vertical re-distribution of CO_2 saturation is observed during equilibration due to low mobility of gas phase. The expected capillary gravity equilibrium is shown not to develop with high accuracy within 260 hours after the initial pressure drop. It also

indicates gas bubbles were not aggregated enough to have sufficient pressure gradients along the vertical dimension to re-distribute.

5. Low relative permeabilities of water and exsolved CO_2 are recorded. The relative permeability of water drops significantly once CO_2 exsolved and remained less than 0.1 after the critical gas saturation is reached; the relative permeability of CO_2 is very low, $10^{-5} \sim 10^{-3}$, even when the exsolved CO_2 saturation increases to over 40%. The low CO_2 mobility is consistent with observations from gas solution drive experiments which had reported gas relative permeability of $10^{-4} \sim 10^{-6}$ (Tang and Firoozabadi 2003, Tang et al. 2006). The high viscosity of oil is considered the main cause of gas mobility reduction but it is not the case in CO_2 exsolution as water is much less viscous. Also no comparably large liquid phase mobility reductions have been reported in solution gas drive experiments. The high interfacial tension between water and CO_2 and the discontinuous CO_2 phase contribute most to the mobility reduction in both water and CO_2 phases.

6. The significant reduction in both water and CO_2 mobility could be favorable for storage security by preventing CO_2 migration or even block possible leakage paths. Studies over much longer time periods than the 260 hours reported here need to be carried out to determine if these low mobilities could persist over years to decades.

Further investigations regarding the temperature effects on CO_2 exsolution phenomenon are needed. Experiments in this report are conducted at $50^{\circ}C$ but as CO_2 saturated brine migrates upwards, the geothermal gradient needs to be taken into account for CO_2 solubility changes. Less CO_2 may exsolve and no exsolution might occur until brine reaches a much shallower depth than in an isothermal condition, since the decrease of temperature compensates for the solubility reduction from pressure drops. Also, the flow properties of CO_2 have fairly strong dependency on temperature.

To verify the low mobility of the exsolved CO_2/ water system, flooding with a CO_2-water solution or pure CO_2 could be conducted to measure the effective permeability of the rock. It would be of great interest to investigate whether the phase mobility measured in a flow driven mainly by exsolution and gas expansion is different from a pressure

gradient driven flow dominated by viscous force. Not only could the relative permeability be measured, but information about the stability of the exsolved CO_2 be obtained. If the exsolved CO_2 phase establishes a very stable low mobility to the water and itself, it would be a favorable feature for geological sequestration projects, since once exsolution occurs somewhere, the exsolved gas will increase the flow resistance in that region and hamper further upward flows or even block the flow path. It would be important to study whether such a negative feedback exists in CO_2 exsolution phenomenon.

Micro model studies are also important to understand how exsolved CO_2 bubbles evolve, aggregate and move in a pore scale. The hypothesis that the presence of disconnected gas bubbles is the main cause of low gas mobility needs to be verified in a microscopic scale. The combination of studies in both core-scale and pore-scale would provide a better understanding of this CO_2 exsolution phenomenon.

Simulations of CO_2 exsolution scenarios in a reservoir scale could also be part of future work. Using the measured relative permeability, case studies can be conducted to investigate how CO_2 exsolution will affect geological sequestration and evaluate whether the low mobility of exsolved CO_2 could be used as part of a remedy for leakage.

References

Akin, S., Kovscek, A.R.: Computed Tomography in Petroleum Engineering Research. In: Akin, S., Kovscek, A.R. (eds.) Applications of X-Ray Computed Tomography in the Geosciences, **215**: 23–38. Geological Society, London (2003) (Special Publications, 0305-8719/03/$15. © The Geological Society of London)

Benson, S.M., Hepple, R.: Prospects for Early Detection and Options for Remediation of Leakage from CO_2 Sequestration Projects. Carbon Dioxide Capture for Storage in Deep Geologic Formations - Results from the CO_2 Capture Project, **2**: Geologic Storage of Carbon Dioxide with Monitoring and Verification, Elsevier Publishing, UK, 1189-1203 (2005)

Benson, S.M., Cole, D.R.: CO_2 Sequestration in Deep Sedimentary Formations. Elements, **4**(5): 325-331 (2008)

El Yousfi, A., Zarcone, C., Bories, S.: Physical Mechanisms for Bubble Growth during Solution Gas Drive. SPE 38921, presented at the SPE Annual Technical Conference and Exhibition, San Antonio, TX, 5-8 October (1997)

Farajzadeh, R., Salimi, H., Zitha, P. L.J., Bruining, H.: Numerical Simulation of Density-driven Natural Convection in Porous Media with Application for CO_2 Injection Projects. International Journal of Heat and Mass Transfer, **50**(25-26): 5054-5064 (2007)

Firoozabadi, A., Kashiev, D.: Pressure and Volume Evolution During Gas Formation in Solution Gas Drive Process. SPE J. 26286, **1**(3): 219-228 (1996)

Firoozabadi, A.: Mechanisms of Solution Gas Drive in Heavy Oil Reservoirs. Journal of Canadian Petroleum Technology, **40**(3):15-20 (2001)

Georgiadis, A., Maitland, G., Trusler, J.P. M., Bismarck, A.: Interfacial Tension Measurements of the (H_2O + CO_2) System at Elevated Pressures and Temperatures. J. Chem. Eng. Data, **55**(10): 4168-4175 (2010)

Hassanzadeh, H., Darvish, M.P., Keith, D.W.: Scaling Behavior of Convective Mixing, with Application to Geological Storage of CO_2. AIChE journal, **53**(5): 1121-1131 (2007)

Hesse, M.A., Tchelepi, H.A., Orr, F.M. Jr.: Scaling Analysis of the Migration of CO_2 in Saline Aquifers. SPE 102796, presented at the SPE Annual Technical Conference and Exhibition, San Antonio, TX, 24-27 September (2006)

Hong, J., Woo, H.S.: Application of the Fractional Derivatives Method to Bubble Growth/Dissolution Processes With or Without First-Order Chemical Reaction. AIChe J., **31**: 1695-1706 (1985)

Juanes, R., Spiteri, E.J., Orr, F.M. Jr., Blunt, M.J.: Impact of Relative Permeability Hysteresis on Geological CO_2 Storage. Water Resour. Res., **42**, W12418, doi:10.1029/2005WR004806 (2006)

King, J.E., Paterson, L.: Role of Convective Mixing in the Long-Term Storage of Carbon Dioxide in Deep Saline Formations. SPE J. 84344, **10**(3): 349-356 (2005)

Krause, M., Perrin, J.C., Benson, S.M.: Modeling Permeability Distributions in a Sandstone Core for History Matching Coreflood Experiments. SPE 126340, presented at the SPE International Conference on CO_2 Capture, Storage, and Utilization, San Diego, CA, 2-4 November (2009)

Leonenko, Y., Keith, D.W.:Reservoir Engineering To Accelerate the Dissolution of CO_2 Stored in Aquifers. Environ. Sci. Technol., **42** (8): 2742–2747 (2008)

Li, X., Yortsos, Y.C.: Critical Gas Saturation: Modeling and Sensitivity Studies. SPE 26662, presented at the SPE Annual Technical Conference and Exhibition, Houston, TX, 3-6 October (1993)

Ohsumi, T., Nakashiki, N., Shitashima, K., Hirama, K.: Density Change of Water due to Dissolution of Carbon Dioxide and Near-field Behavior of CO_2 from a Source on Deep-sea Floor. Energy Conversion and Management, **33**(5-8): 685-690 (1992)

Perrin, J.C., Benson, S.M.: An Experimental Study on the Influence of Sub-Core Scale Heterogeneities on CO_2 Distribution in Reservoir Rocks. Transport in Porous Media, DOI: 10.1007/s11242-009-9426-x, **82**(1): 93–109 (2010)

Riaz, A., Hesse, M.A., Tchelepi, H.A., Orr, F.M. Jr.: Onset of Convection in a Gravitationally Unstable Diffusive Boundary Layer in Porous Media. Journal of Fluid Mechanics, **548**: 87-111 (2006)

Riaz, A., Tchelepi, H.A.: Dynamics of Vertical Displacement in Porous Media Associated With CO_2 Sequestration. SPE J. 103169, **13**(3):305-313 (2008)

Saadatpoor, E., Bryant, S.L., Sepehrnoori, K.: New Trapping Mechanism in Carbon Sequestration. Transport in Porous Media, DOI: 10.1007/s11242-009-9446-6, **82**(1): 3-17 (2010)

Silin, D., Patzek, T. W., Benson, S. M.: A one-dimensional model of vertical gas plume migration through a heterogeneous porous medium. International Journal of Greenhouse Gas Control (2008). ISSN 1750-5836, DOI: 10.1016/j.ijggc.2008.09.003

Smith, G.E.: Fluid Flow and Sand Production in Heavy Oil Reservoirs Under Solution Gas Drive. SPE Production Engineering, **3**(2):169-180 (1988)

Tang, G.Q., Firoozabadi, A.: Gas- and Liquid-Phase Relative Permeabilities for Cold Production from Heavy Oil Reservoir. SPE Reservoir Evaluation & Engineering, **6**(2):70-80 (2003)

Tang, G.Q., Sahni, A., Gadelle, F., Kumar, M., Kovscek, A.R.: Heavy-oil Solution Gas Drive in Consolidated and Unconsolidated Rock. SPE J. 87226, **11**(2): 259-268 (2006)

Wilt, P.M.: Nucleation Rates and Bubble Stability in Water Carbon Dioyde Solutions. J. Coll. Int. Sci., **112**: 530-538 (1989)

Zhang, Y.Q., Oldenburg, C.M.,Benson, S.M.: Vadose Zone Remediation of Carbon Dioxide Leakage from Geologic Carbon Dioxide Sequestration Sites. Vadose Zone Journal, **3**:858-866 (2004)